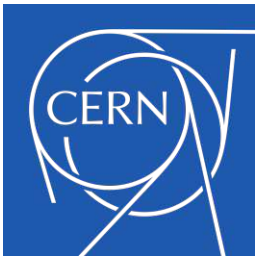

Diplomarbeit

Resonance identification and compensation studies to minimize losses for high intensity beams in the PSB

zur Erlangung des akademischen Grades

Diplom-Ingenieur

im Rahmen des Studiums

Technische Physik

eingereicht von

Dipl.-Ing. Daniel Zeitz
Matrikelnummer 11701845

ausgeführt am Atominstitut
der Fakultät für Physik der Technischen Universität Wien
in Zusammenarbeit mit CERN

Betreuung:
Privatdoz. Dipl.Ing. Dr.techn. Michael Benedikt
Foteini Asvesta, PhD (CERN)

Wien, 13.04.2024

Daniel Zeitz	Michael Benedikt

Statuatory Declaration

I herewith declare that I have composed the present thesis myself and without use of any other than the cited sources and aids. Sentences or parts of sentences quoted literally are marked as such; other references with regard to the statement and scope are indicated by full details of the publications concerned. The thesis in the same or similar form has not been submitted to any examination body and has not been published. This thesis was not yet, even in part, used in another examination or as a course performance. Furthermore I declare that the submitted written (bound) copies of the present thesis and the version submitted on a data carrier are consistent with each other in contents.

Place, Date: Signature:

Acknowledgments

Throughout the writing process of this thesis I have been very fortunate to receive a great deal of support, from the colleagues at CERN, from my friends both in Geneva and in Vienna and from my family.

First of all, I want to thank my supervisor at CERN, Foteini Asvesta, who gave me the opportunity to do this amazing internship, who was always open for questions and helped me with her invaluable expertise. You allowed me to stay on the right path and allowed me to gain great insight into the exciting field of accelerator physics.

I would also like to thank the other members of the INC section as well as the ABP group for the interesting presentations and discussions during breaks or the MD sessions. In particular, I want to thank Tirsi for his constant support and kind guidance during the many MD sessions in the CCC as well as the PSB operators for doing such a great job at keeping the PSB running. I would also like to thank the other technical students that I got to know both during and after working hours in R1 for the fun times and helping me get my mind off of work. I also want to thank the other students from St.Boniface as well as all other friends in Geneva for making this year even more memorable.

Last but not least, I want to thank Michael Benedikt for supervising this thesis from the Vienna University of Technology's side.

Finally, I would like to thank my parents and my sister Vicki who are always there for me, for supporting and guiding me throughout my studies.

Contents

Kurzfassung

Der Proton Synchrotron Booster (PSB) besteht aus vier übereinander gestapelten Ringen und ist der erste Vorbeschleuniger des Large Hadron Collider (LHC), dem derzeit grössten Teilchenbeschleuniger der Welt. Entlang des LHC befinden sich vier große Experimente wo Protonenstrahlen kollidieren. Um eine hohe Kollisionsrate zu haben, benötigt man Strahlen mit möglichst hoher Brillanz, was bedeutet, dass sich möglichst viele Teilchen in einem möglichst kleinen Phasenraumvolumen befinden. Das Problem ist, dass die elektromagnetische Wechselwirkung zwischen Protonen zu einer inkohärenten Verschiebung der Betatronschwingungszahl ("Tune") im Strahl führt. Diese Verschiebung ("Tune Shift") ist bei niedrigen Energien erhöht und da die Injektionsenergie im PSB bei $160\mathrm{MeV}$ liegt, dominiert dieser Effekt im PSB und der Tune Shift $\Delta Q_{x,y} \approx -0.6$. Um hohe Brillanz zu gewährleisten, muss der Tune des Strahls viel höher als der ganzzahlige Tune liegen. Bei der Einspeisung der Protonen ist der eingestellte Tune in einem Bereich, welcher eine hohe Dichte an Resonanzen aufweist. Durch den grossen Tune Shift werden dabei viele Resonanzen überlappt, was zu einem Anstieg der Emittanz sowie Verlusten führt. Mit steigender Energie sinkt der durch Raumladungseffekte erzeugte Tune Shift, weshalb während der Beschleunigung der Tune dann in eine resonanzfreie Zone verschoben wird, um den Strahl dort zu extrahieren. Diese Resonanzen werden unter anderem durch Inhomogenitäten in Magnetfeldern, Fehlausrichtungen von Magneten und Randfeldern getrieben. Die Abweichungen vom idealen Magneten sind in jedem der vier Ringe des PSB unterschiedlich und müssen daher individuell kompensiert werden. Diese Diplomarbeit behandelt die Identifikation und Kompensation der Resonanzen dritter und vierter Ordnung in allen Ringen des PSB.

Der verwendete Ansatz basiert auf der Minimierung der Verluste, wenn eine Resonanz durchkreuzt wird. Um individuelle Resonanzen zu durchkreuzen, wird ein Strahl mit hoher Emittanz und niedriger Intensität in den PSB eingespeist. Dadurch ist der Tune Shift im Vergleich zu den hoch brillanten LHC Strahlen stark reduziert und der Strahl wird nur durch eine einzelne Resonanz beeinflusst. Die Verluste, wenn eine Resonanz durchkreuzt wird, werden gemessen und mithilfe von geeigneten Korrektormagneten können diese Verluste reduziert werden bzw. werden in der richtigen Einstellung keine Verluste mehr beobachtet. Dies ist genau dann der Fall, wenn die gekreuzte Resonanz kompensiert wurde. Alle Resonanzen dritter und vierter Ordnung können individuell vollständig kompensiert werden. Basierend auf der individuellen Resonanzkompensation kann im weiteren Verlauf analytisch eine Konfiguration von Korrektormagneten gefunden werden, welche alle Resonanzen global kompensiert. Da der PSB aus vier übereinander liegenden Ringen besteht und die Resonanzen in jedem Ring unterschiedlich sind, variiert der Grad der Kompensation je nach Ring. Im Durchschnitt konnten die Verluste durch Resonanzen auf weniger als 4% reduziert werden.

Abstract

The CERN Proton Synchrotron Booster (PSB) is the first synchrotron in the Large Hadron Collider (LHC) injector chain and is composed of four superposed rings. High brightness beams, delivered by the PSB, are required in order to have a high collision rate at the interaction points where the physics experiments are located. In combination with the low injection energy of $160\mathrm{MeV}$, the PSB is operating in a space charge dominated regime. Space charge causes the particles in the PSB to have a large tune spread with a maximum tune shift of up to $\Delta Q_{x,y} \approx -0.6$ and in order to optimize brightness, the transverse tunes are set to high values far from the integer tune. At injection, the tune is in a resonance dominated zone where many resonances are overlapped by the tune spread. Overlapping excited resonances causes an increase of emittance (blow-up) as well as losses of high amplitude particles. As the space charge induced tune spread shrinks during acceleration, the tune is moved to the extraction working point in a resonance free zone. In order to move the tune to the extraction working point, high order resonances have to be crossed which causes further blow-up and losses. These resonances are driven by magnet imperfections, which are different in each ring. This thesis aims at describing the process of 3^{rd} and 4^{th} order resonance identification and compensation in the PSB.

The approach used in this study is based on loss minimization when crossing a resonance. In order to cross individual resonances, low intensity beams were blown up at injection using the stripping foil. This causes them to have a small tune spread which limits the interaction with other resonances. Then, the tune is changed in a way that only one resonance is crossed and the losses during the crossing are measured. Using suitable corrector magnets, which affect the crossed resonance, the induced losses can be altered and, in the right configuration, completely negated. It was shown that all individual 3^{rd} and 4^{th} order resonances can be fully compensated in all rings. Further, using a global resonance compensation scheme based on the individual resonance compensation settings, it was possible to significantly reduce the beam losses when crossing all 3^{rd} and 4^{th} order resonances. The degree of resonance compensation varies among the rings and on average the remnant losses can be reduced to less than 4%.

Chapter 1

Introduction

The current model in particle physics, the Standard Model, has been developed over the last 70 years and has been a combined effort in theoretical and experimental physics. The experiments, allowing for the discovery of some of the most important particles, are possible due to the construction of the Large Hadron Collider (LHC)[1]. The LHC is the last element of the accelerator complex at CERN[2], which consists of four main synchrotrons, whose goal is to accelerate protons or ions close to the speed of light. A synchrotron is a circular machine in which charged particles can be kept on a stable orbit while being accelerated, allowing them to carry more energy. After particles have been accelerated in the first three synchrotrons, they are injected into the LHC in two counter-rotating beams on two different orbits. These can be deviated and brought together using strong dipole magnets to collide at four interaction points. At collision, the energy they carry is released and for a split second the temperature at the collision point is over 200,000 times hotter than the core of the sun. This energy is freed to form particles, which can then be detected by the experiments situated around the collision points. In order to have a high rate of collisions, the beams have to be very bright, carrying a lot of energy in a very small space.

The Proton Synchrotron Booster (PSB) is the first synchrotron in the injector chain of the LHC, which is currently the largest and most powerful proton synchrotron in the world. The PSB is composed of four superposed rings with a circumference of 157 m. H^- ions from LINAC4[2] are injected into the PSB and the protons are then separated from the H^- ions through a stripping foil that strips electrons. The protons are injected into the PSB at an energy of $160\mathrm{MeV}$ and accelerated over 530 ms up to $2\mathrm{GeV}$. The high intensity beams are then sent to the isotope facility ISOLDE[3] or are further accelerated in the LHC injection chain. In order to keep the most particles throughout the LHC injection chain, resulting in high brightness beams in the LHC, beam blow-up and losses have to avoided as much as possible.

At the relatively low injection energy, space-charge is a dominant electromagnetic interaction between particles in the beam which causes a strong, incoherent negative tune shift[4]. This causes particles to interact with resonances, which are driven among other sources by magnet errors and misalignments in the magnet lattice[5, 6]. This interaction causes an increase in beam emittance and losses in intensity[6–9]. In order to maximize beam brightness, the working point in tune space at injection is thus set far away from the integer tune. As the

protons are accelerated, the tune shift due to space charge shrinks[10] and the tune is moved to a working point in a resonance free zone in tune space, at which the beam will be extracted. During this tune change, many resonance lines are crossed which causes an inevitable interaction of high amplitude particles with resonances. In order to achieve high brightness beams for the LHC, it is necessary to minimize the interaction with excited resonances by compensating them. Using different types of corrector magnets allows for the compensation of individual resonances. The compensating corrector magnet configuration differs from ring to ring as the magnet imperfections which drive the higher order resonances vary in each ring.

The resonance excitation can be characterized with a complex number called the resonance driving term (RDT). The amplitude and phase of the resonance driving term of any set of corrector magnets in the ring can be calculated analytically and, in combination with the experimentally acquired compensating corrector magnet configuration, one can represent how individual resonances are driven by certain magnets. All individual resonances can be fully compensated but as the corrector magnets used in this study drive multiple resonances simulaneously, the compensation of one resonance might enhance another. In order to compensate all resonances simultaneously, a global resonance compensation configuration using more corrector magnets can then be determined based on the individual resonance compensation settings. The scope of this thesis will be individual and global resonance compensation of the excited 3^{rd} and 4^{th} order resonances in all rings using the available set of corrector magnets.

Chapter 2

Theoretical Background

2.1 Transverse beam dynamics

The particles motion in the PSB (as well as in all other accelerators at CERN) is described by using a Frenet-Serret Coordinate System, which is a right-handed coordinate system moving along the particles equilibrium orbit shown in Figure 2.1. The particles position at any time can be described by the vector $\vec{r} = \vec{r_0} + x\hat{x} + y\hat{y}$.

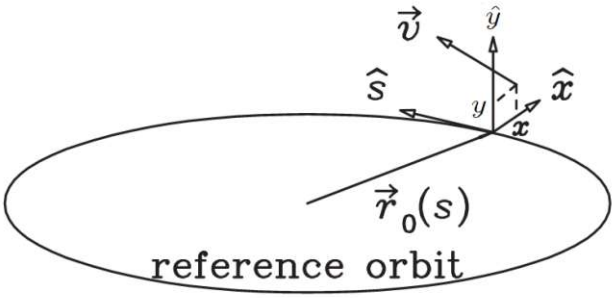

Figure 2.1: Frenet-Serret Frame adapted from [10].

The coordinates x and y describe the particles position on the horizontal and vertical axes respectively. The coordinate s is tangential to the circular trajectory and is used to describe the longitudinal position along the orbit.

The motion of protons in the particle accelerator is governed by the Lorentz force,

$$\vec{F_L} = \frac{d\vec{p}}{dt} = e(\vec{E} + \vec{v} \times \vec{B}), \tag{2.1}$$

where $\vec{p}$ is the particle's momentum, $e = 1.602 \times 10^{-19}$ is the elementary charge[11], $\vec{E}$ is the electric field, $\vec{v}$ is the particles velocity and $\vec{B}$ is the magnetic field[10]. The electric field can transfer energy to the particles and accelerate them in the longitudinal direction, while the magnetic field is used to steer the beam, i.e. changing it's direction in the transverse plane. For the scope of this study pure transverse motion can be assumed, hence the electric field will be zero in the following theoretical treatment of beam dynamics and resonances.

Dipole magnets bend the particles inwards and keep them on an ideal circular orbit, which is called the

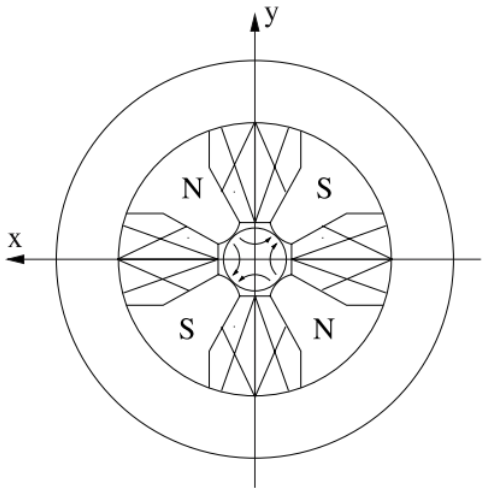

Figure 2.2: Schematic representation of a quadrupole magnet from [12].

design orbit. The ideal design orbit of a particle with momentum $\vec{p}$ and charge q is described by the beam rigidity

$$\vec{B}\rho = \frac{\vec{p}}{q}, \tag{2.2}$$

which is a parameter of the synchrotron with the invariable bending radius ρ and the main dipole magnetic field $\vec{B}$. Actual particle motion deviates from this design orbit and the coordinates (x, y) describe the transverse deviation from the design orbit. In order to keep the particles trajectories close to the design orbit, focusing quadrupole lenses are used. These quadrupoles generate a magnetic field that increases linearly with the distance to the magnet center,

$$\vec{B} = g(x\hat{x} + y\hat{y}), \tag{2.3}$$

where g is the magnetic field gradient, and x and y are the horizontal and vertical planes respectively[10]. These quadrupoles act as focusing lenses exerting stronger focusing on protons the further away they are from the design orbit, effectively readjusting their trajectories towards the design orbit.

A transverse representation of a quadrupole magnet can be seen in Figure 2.2. The forces acting on a proton with velocity v in both transverse planes can be calculated using the Lorentz equation 2.1 which yields:

$$\vec{F} = evg\hat{s} \times (x\hat{x} + y\hat{y}) = -evgy\hat{y} + evgx\hat{x}. \tag{2.4}$$

This force shows that a horizontally focusing quadrupole is simultaneously a vertically defocusing quadrupole. Alternating between focusing and defocusing quadrupoles allows for net focusing in both planes[10]. These two types of quadrupoles along with dipoles constitute the so-called FODO cell which will be repeated periodically along the ring[13]. Further elements that are part of this cell are sextupoles, various corrector magnets, and elements for beam instrumentation and monitoring. A schematic representation of a $\frac{1}{2}$-FODO cell can be seen in Figure 2.3.

It is more convenient to normalize the quadrupole gradient g to the particles momentum p which increases

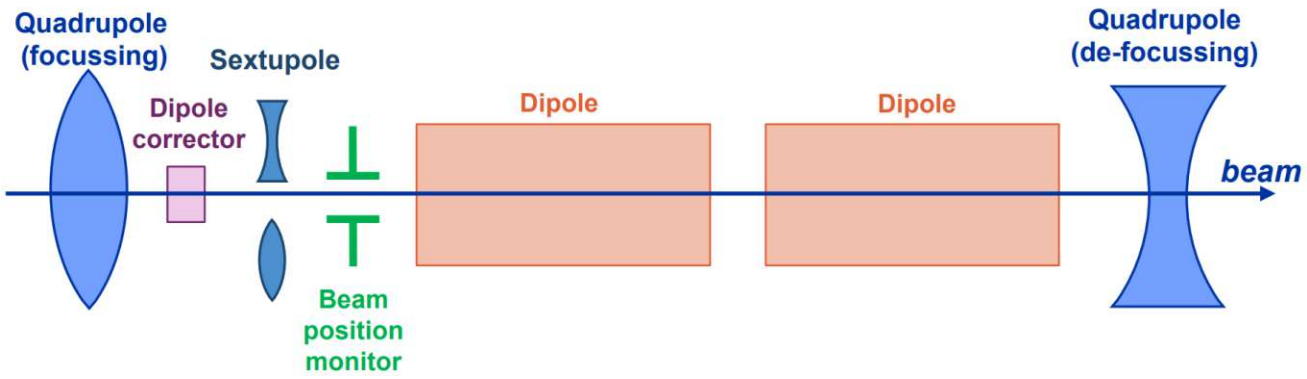

Figure 2.3: Schematic representation from [14] of a $\frac{1}{2}$-FODO cell, made up of a focusing and defocusing quadrupole along with sextupoles for chromaticity correction, a dipole corrector for orbit correction and a beam position monitor.

during acceleration. Thus, the normalized quadrupole gradient $k = \frac{g}{p/q}$, that remains constant throughout the cycle, will be used instead.

Assuming only small deviations from the design orbit and no momentum spread, the equations of motion in the horizontal and vertical plane are[10]:

$$x''(s) + \left(k(s) + \frac{1}{\rho^2}\right) x(s) = 0, \tag{2.5}$$

$$y''(s) - k(s)y(s) = 0. \tag{2.6}$$

The additional factor $\frac{1}{\rho^2}$ is necessary to account for the weak focusing effect of the dipole magnets which bends particles. This factor is usually small in high energy accelerators. These differential equations are called Hill's equations and describe an oscillation in the transverse plane, which is called betatron oscillation. The solution of Hill's equation in each of the planes is of the following form:

$$x(s) = \sqrt{\epsilon}\sqrt{\beta(s)} \cdot \cos(\Psi(s) + \phi) \tag{2.7}$$

where the emittance ϵ and the phase ϕ are integration constants. The beta function $\beta_{x,y}(s)$ depends on the arrangement of quadrupoles in the ring. The beta functions in both planes in a section of the PSB are represented in Figure 2.4. The beta function defines the beam envelope which defines the maximum amplitude of a particle and is used to describe the beam size.

As the quadrupoles in the ring do not change their position in the synchrotron, the beta function is periodic with the synchrotron length L, i.e. $\beta(s) = \beta(s + L)$. The phase advance after the distance s in the ring,

$$\Psi(s) = \int_0^s \frac{ds'}{\beta(s')}, \tag{2.8}$$

can be used to define the tune Q, which is the number of betatron oscillations normalized to 2π after a full

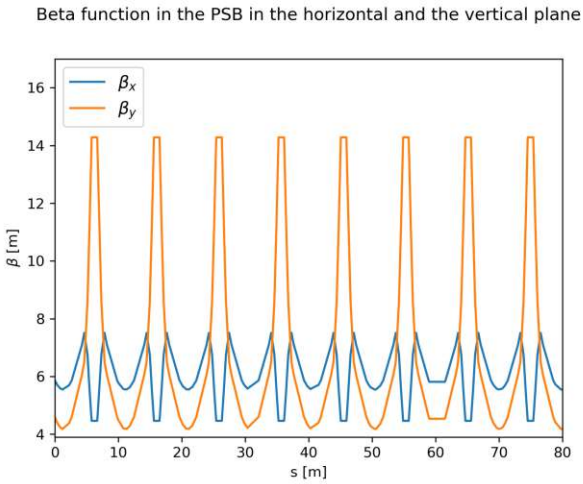

Figure 2.4: Beta functions in a segment of the PSB in the horizontal and vertical planes.

revolution in the ring:

$$Q = \frac{1}{2\pi} \oint \frac{ds'}{\beta(s')}. \tag{2.9}$$

In phase space, the particles trajectory is an ellipse which can be seen in Figure 2.5. The shape of this ellipse is defined by two parameters, $\alpha = \frac{-\beta'(s)}{2}$ and $\gamma = \frac{1+\alpha(s)^2}{\beta(s)}$. These so-called Twiss parameters α, β, γ are used to define the Courant-Snyder invariant:

$$\epsilon = \gamma(s)x(s)^2 + 2\alpha(s)x(s)x'(s) + \beta(s)x'(s)^2. \tag{2.10}$$

The emittance is a conserved quantity and defines the area of the ellipse which is $\epsilon\pi$. The betatron oscillations correspond to revolutions of the particles along the elliptic trajectory in phase space.

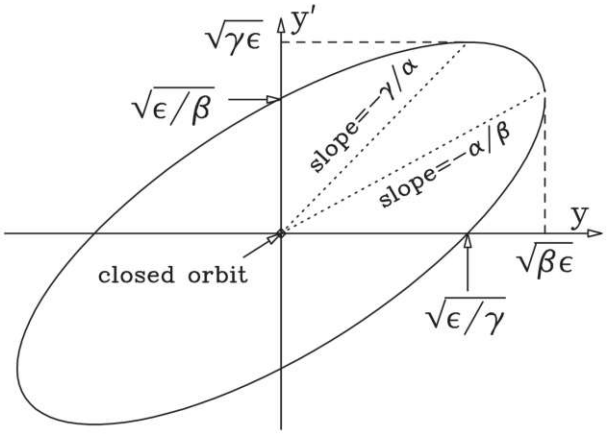

Figure 2.5: Trajectory of a single particle in phase space with the Twiss parameters defining the shape and the orientation of the ellipse. Figure adapted from [10].

Particles in the beam have a momentum spread $\frac{\Delta p}{p}$, and as particles with greater momentum will experience

a stronger centrifugal force, they will be on a larger orbit larger than the design orbit. The relation between the varied orbit length and the momentum spread is given by the dispersion function $D(s)$. The solution of Hill's equations of motion 2.7 is only valid if there is no momentum spread and all particles are on the design orbit. In order to take dispersion into account, the solution has to be modified as follows[10]:

$$x(s) = x_\beta(s) + D(s) \cdot \frac{\Delta p}{p}, \tag{2.11}$$

where x_β is equation 2.7.

In addition to the altered orbit radius, momentum spread will also cause a tune spread ΔQ of the particles as particles with different momentum will be focused differently. Particles with higher momentum will be focused less than particles with lower momentum as can be seen in Figure 2.6 on the left. This in turn will affect the phase advance Ψ for particles with different momentum, resulting in a tune spread in the beam. The relation between the momentum spread and the tune spread is given by

$$\Delta Q_{x,y} = Q'_{x,y} \cdot \frac{\Delta p}{p}, \tag{2.12}$$

where Q' is the chromaticity which is defined as

$$Q' = -\frac{1}{4\pi} \oint k(s)\beta(s)ds. \tag{2.13}$$

This chromaticity-induced detuning can be compensated using sextupole magnets[10]. By introducing sextupoles after quadrupoles, particles are sorted based on their momentum, ensuring convergence at the same focal point, which reduces the tune spread. The difference in focusing with and without sextupole magnets is represented schematically in Figure 2.6.

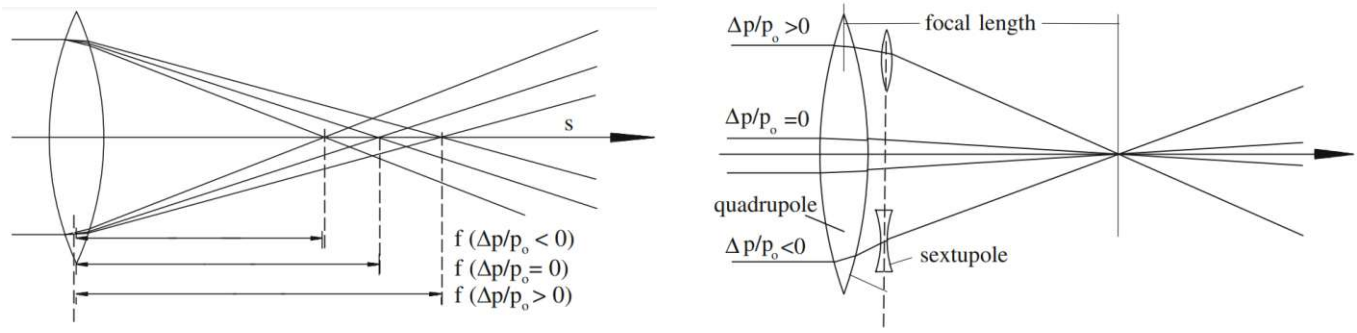

Figure 2.6: Focusing of beam on different orbits without sextupoles (left) and with sextupoles(right) from [12].

Another effect causing detuning of the particles is space charge, which is the electromagnetic interaction between charged particles in a beam. The maximum tune shift for particles at the center of the bunch is [15]:

$$\Delta Q_{x,y} = -\frac{r_0 \lambda}{2\pi e \beta^2 \gamma^3} \oint \frac{\beta_{x,y}(s)}{\sigma_{x,y}(s)(\sigma_x(s) + \sigma_y(s))} ds \,, \tag{2.14}$$

where r_0 is the classical radius of the particle, λ the longitudinal line density, e the elementary charge, $\beta = \frac{v}{c}$ and $\gamma = \frac{1}{\sqrt{1-\beta^2}}$ the relativistic factors, $\beta_{x,y}$ the transverse β-functions and $\sigma_{x,y}$ the transverse beam sizes.

The tune spread decreases with energy, which can be deduced from 2.14. For LHC beams, the tune spread at extraction energy is significantly lower than at injection energy, which is shown in Figure 2.7 where the tune spread at different energies has been estimated analytically with [4].

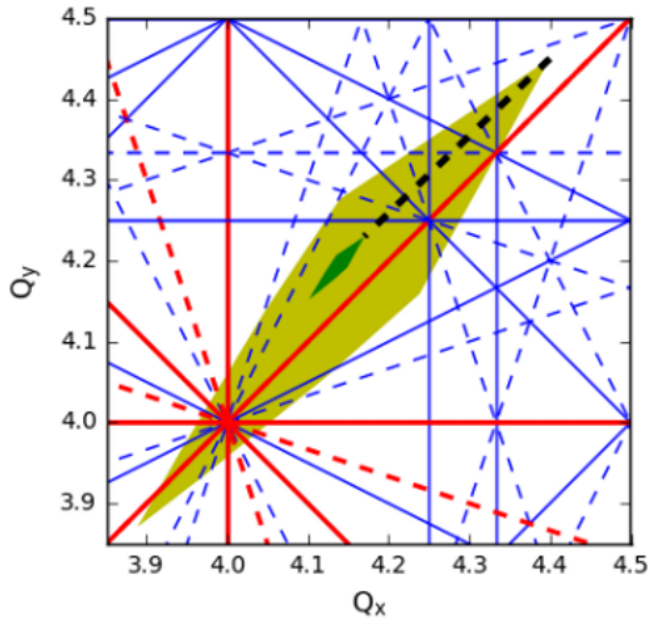

Figure 2.7: Space charge induced incoherent tune spread at injection energy (yellow) and at extraction energy (green). The black dashed line indicates the tune change from the working point at injection to the working point at extraction. Figure adapted from [16].

The beam dynamics in a linear lattice can be described using the following Hamiltonian[10]:

$$\mathcal{H} = \frac{1}{2}(k_x x^2 + k_y y^2 + p_x^2 + p_y^2), \tag{2.15}$$

where $k_{x,y}$ are the normalized magnetic field gradients and $p_{x,y}$ the momenta in both planes. The Hamiltonian can be transformed from the canonical phase space coordinates (x, y, p_x, p_y) to a new set of variables called action $J_{x,y}$ and angle (phase) $\phi_{x,y}$ using the Floquet transformation[10]

$$u = \sqrt{2J_u \beta_u} \cdot \cos(\Psi_u), \tag{2.16}$$

$$u' = -\sqrt{\frac{2J_u}{\beta_u}} \cdot [\sin(\Psi) + \alpha \cos(\Psi)], \tag{2.17}$$

with u being x or y and α and β being the Twiss parameters.

The Hamiltonian 2.15 in action-angle variables can then be written as

$$\mathcal{H} = \frac{1}{R}(Q_x J_x + Q_y J_y), \tag{2.18}$$

with the radius R of the ring and the tunes $Q_{x,y}$.

The solutions of Hills equation can also be rewritten in terms of action-angle variables:

$$x(s) = \sqrt{2J_x\beta_x(s)} \cdot \cos(\Psi_x(s) + \phi) + D(s) \cdot \frac{\Delta p}{p}, \tag{2.19}$$

$$y(s) = \sqrt{2J_y\beta_y(s)} \cdot \cos(\Psi_y(s) + \phi), \tag{2.20}$$

with the emittance $\epsilon = 2J$.

2.2 Resonances

There are many magnet imperfections which have to be taken into account as they affect the beam dynamics and drive resonances which cause emittance blow-up and, for high amplitude particles, losses. These imperfections can be for example misaligned magnets or fringe fields, which induce additional multipolar fields. Further, in order to compensate for chromaticity, sextupoles have to be used in the machine. These sextupoles have non-linear magnetic fields which drive higher order resonances. A schematic representation of a sextupole magnet and its magnetic field can be seen in Figure 2.8.

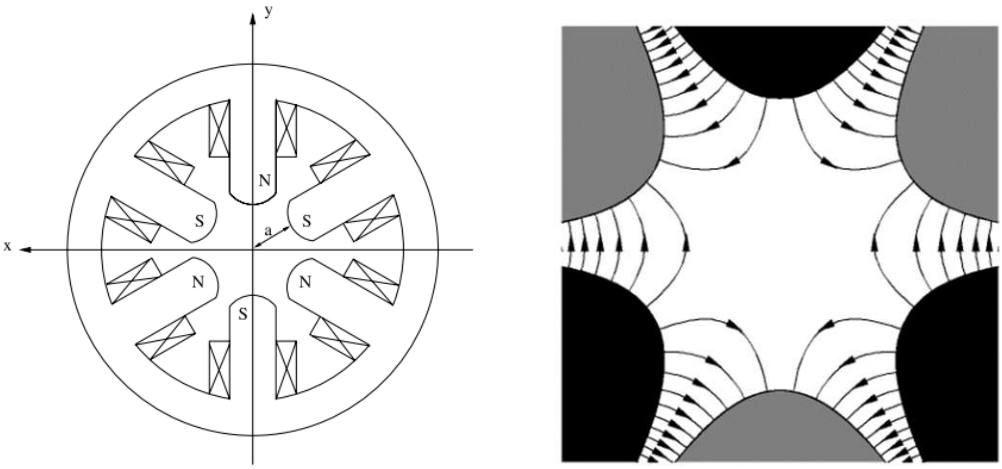

Figure 2.8: Left: Schematic transverse representation of a sextupole magnet adapted from [17]. Right: Magnetic field of a sextupole magnet adapted from [14].

In order to account for higher order magnetic fields, a more general description of the magnetic field is

necessary. Including higher order multipoles, the magnetic field is expressed using the multipole expansion:

$$B_y + iB_x = B_0 \sum_{n=0}^{\infty} (b_n + ia_n)(x + iy)^n \tag{2.21}$$

$$b_n = \frac{1}{B_0 n!} \frac{\partial^n B_y}{\partial x^n}, \qquad a_n = \frac{1}{B_0 n!} \frac{\partial^n B_x}{\partial x^n} \tag{2.22}$$

where a_n and b_n represent the $2(n+1)$th skew and normal multipole coefficients respectively. A skew magnet is rotated by an angle $\frac{\pi}{2n}$ with respect to the normal magnet. In this thesis, multipoles up to order $n = 4$, i.e. octupoles, are considered. The explicit magnetic field containing contributions up to octupoles can be expressed as follows:

$$B_y = b_0 + b_1 x - a_1 y + b_2(x^2 - y^2) - a_2 xy + b_3(x^3 - 3xy^2) - a_3(-y^3 + 3x^2 y) \tag{2.23}$$

$$B_x = \underbrace{a_0}_{Dipole} + \underbrace{a_1 x + b_1 y}_{Quadrupole} + \underbrace{a_2(x^2 - y^2) + b_2 xy}_{Sextupole} + \underbrace{a_3(x^3 - 3xy^2) + b_3(-y^3 + 3x^2 y)}_{Octupole} \tag{2.24}$$

$$\tag{2.25}$$

The non-linear magnetic field components from 2.24 that arise from multipolar errors in the machine drive higher order resonances. As the PSB is operating in a space-charge dominated regime, there is strong detuning of the particles which causes inevitable interaction of the beam with excited higher order resonances. This interaction can be observed through an increase in beam emittance and particle losses if the tunes $Q_{x,y}$ is close to the resonance condition:

$$mQ_x + nQ_y = l, \tag{2.26}$$

with m, n being integers, l being the harmonic and $|m| + |n|$ being the order of the resonance. The PSB is made up of 16 identical cells, which means the periodicity of the lattice $P = 16$. If the harmonic l is an integer multiple of P, then the resonance is called systematic. Systematic resonances are driven by errors that are evenly distributed in every cell and their kicks will add up constructively. Otherwise, resonances that are driven by errors that are randomly distributed along the ring are called non-systematic. The resonance lines where the resonance condition up to 4^{th} order is fulfilled can be seen in Figure 2.9. Normal and skew multipoles drive normal and skew resonances respectively.

The Hamiltonian in action-angle coordinates including the non-linear terms of the magnet lattice is[14]

$$\mathcal{H} = \frac{1}{R}(Q_x J_x + Q_y J_y) + V(J, \phi, s), \tag{2.27}$$

$$V(J, \phi, s) = \frac{\epsilon}{R} \sum_{j=0}^{m_x} \sum_{l=0}^{m_y} J_x^{\frac{j+k}{2}} J_y^{\frac{l+m}{2}} h_{jklm} e^{i[(j-k)\phi_x + (l-m)\phi_y]}, \tag{2.28}$$

with the radius of the ring R, the emittance ϵ, the tune $Q_{x,y}$, the action $J_{x,y}$ and the phase advance $\phi_{x,y}$ in the

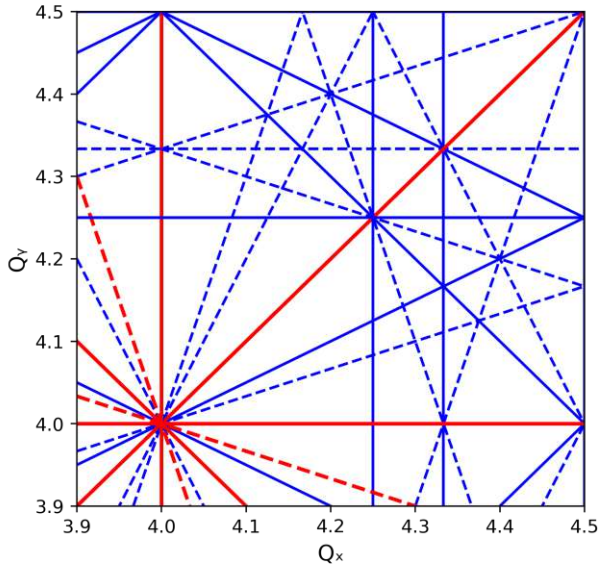

Figure 2.9: Resonance lines of resonances up to 4^{th} order, with normal resonances in solid lines, skew resonances in dashed lines. Systematic resonances are plotted in red and non-systematic resonances are plotted in blue.

horizontal and vertical plane respectively. The first term on the left-hand side of 2.27 corresponds to the linear lattice while the perturbation V contains the non-linear magnetic fields which drive higher order resonances. The complex coefficients h_{jklm} in Eq. 2.28 are called the resonance driving terms. The indices j, k, l, m are part of a more generalized form of the resonance condition2.26:

$$(j-k)Q_x + (l-m)Q_y = n. \tag{2.29}$$

This equation describes more types of resonances which are explained in further detail in [10, 12], but go beyond the scope of this study. Instead, the focus lies on resonances where k and m are both equal to zero, in which case the resonance condition simplifies into 2.26.

3^{rd} order resonances

The pertubating potential 2.28 is a periodic function of s and can be expressed as a Fourier series [18] with the Fourier harmonics corresponding to different resonances. For this study, two normal and skew 3^{rd} order resonances are considered, the normal $3Q_x = 13$ and $Q_x + 2Q_y = 13$ resonances and the skew $3Q_y = 13$ and $2Q_x + Q_y = 13$ resonances. For each of these resonances, an individual perturbating term can be found[10]. For example the case of the resonance $3Q_x = l$, the Hamiltonian with the pertubation term is

$$\mathcal{H} = \frac{1}{R}(Q_x J_x + Q_y J_y) + G_{3,0,l} J_x^{3/2} \cos(3\phi_x - l\theta + \xi_{3,0,l}), \tag{2.30}$$

with $G_{3,0,l}$ being the amplitude and $\xi_{3,0,l}$ the phase of the resonance driving term, $\theta = \frac{s}{R}$ being the orbiting angle with R being the radius of the PSB. The resonance driving term can then be further expressed as

$$G_{3,0,l}e^{j\xi_{3,0,l}} = \frac{\sqrt{2}}{24\pi}\oint \beta_x^{3/2}K_2(s)e^{j[3\chi_x(s)-(3Q_x-l)\theta]}ds, \tag{2.31}$$

with the normalized sextupole magnet strength $K_2(s)$, the beta function β_x, the phase advance $\chi_x(s) = \int_0^s \frac{ds}{\beta_x}$. The amplitude and the phase of the resonance driving term of a corrector magnet at a given position s with a normalized magnet strength $K_2(s)$ and the beta function $\beta_x(s)$ can be calculated using PTC[19] in MADX[20]. The corrector magnet strengths $K_2(s)$ that compensate a certain resonance were identified experimentally, allowing for the representation of the compensating RDTs for each resonance in all rings.

4^{th} order resonances

Excitation of 4^{th} order resonances has not been observed before the LIU. The 4^{th} order resonances that are excited are $4Q_x = 17$, $2Q_x + 2Q_y = 17$ and $4Q_y = 17$. Using MADX[20], it can be calculated how any of the octupole corrector magnets drive the 4^{th} order resonances. Similarly to the case of the 3^{rd} order resonances, the experimentally acquired octupole strengths that compensate the resonance can be used to calculate and represent the compensating RDT.

Chapter 3

Resonance Compensation

The approach used for individual resonance compensation aims at minimizing the losses when crossing that resonance. This has been done in previous studies on resonance compensation in the PSB [5, 21–23] as well as in other proton synchrotrons[24–26]. The excited resonances were identified in each ring with dynamic tune scans which have been performed in 2021[27]. During these scans, the tune in one plane is kept constant while the tune in the other plane is varied, which allows for mapping out of the loss rates in tune space when different resonances are crossed. The excited resonances in all rings can be seen in Figure 3.1.

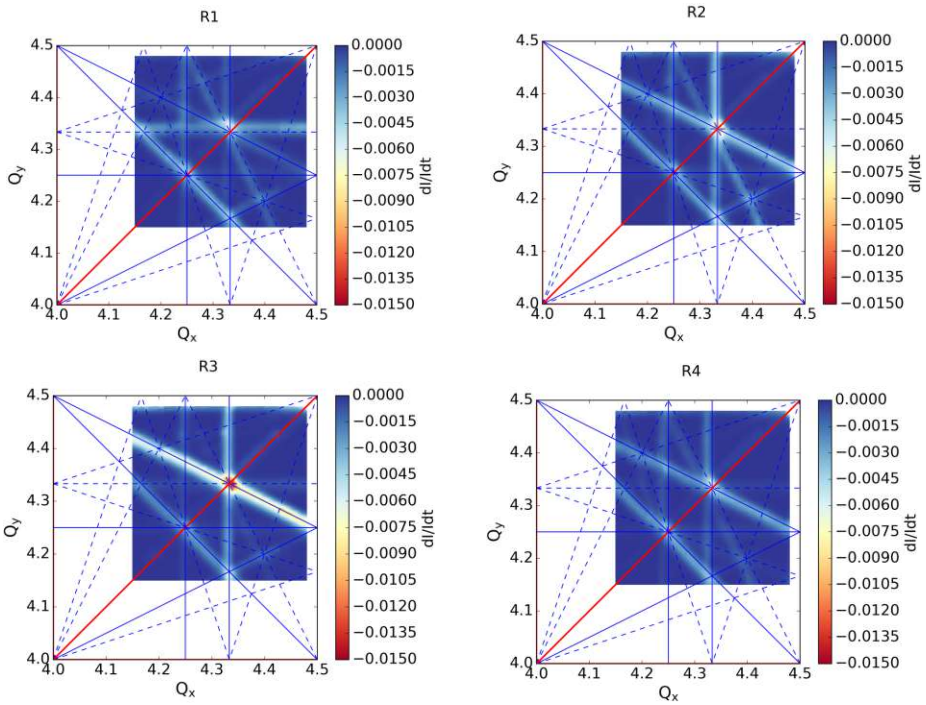

Figure 3.1: Loss rates in transverse tune space in all four rings of the PSB obtained from dynamic tune scans from 2021[27]. The loss rate, which corresponds to the resonance excitation strength, is color-coded in tune space. Resonance lines up to 4^{th} order are plotted, normal resonances in solid lines and skew resonances in dashed lines. Non-systematic resonances are plotted in blue and systematic resonances in red.

The scope of the following section will be the individual compensation of each of these excited resonances using pairs of corrector magnets as it has been done in the past[5]. However, as these corrector magnets drive multiple resonances, compensating one might enhance another. Thus, in order to compensate all excited resonances simultaneously, a global resonance compensation scheme using a set of more corrector magnets will be described in the later section.

3.1 Individual resonance compensation

As high intensity beams in the PSB at injection energy have a very high tune spread due to space charge, they are not suitable to compensate individual resonances, as the beam would be affected by multiple resonances simultaneously. In order to eliminate the effect of other resonances, a low intensity and high emittance beam is used when compensating individual resonances. This beam has low brightness and a much smaller tune spread than the high brightness beams for the LHC. It is thus sufficiently small to cross a resonance without being affected by any other resonances, as can be seen in Figure 3.2. The area where each of the normal and skew resonances are crossed can be seen in Figure 3.3. In order to have an unchanged resonance throughout the crossing, the entire cycle is at flat bottom energy of 160MeV with a constant magnetic field for the entire study and the resonance crossing takes about 250ms, which enhances the interaction of the entire bunch with the resonance and increases the sensitivity for the losses.

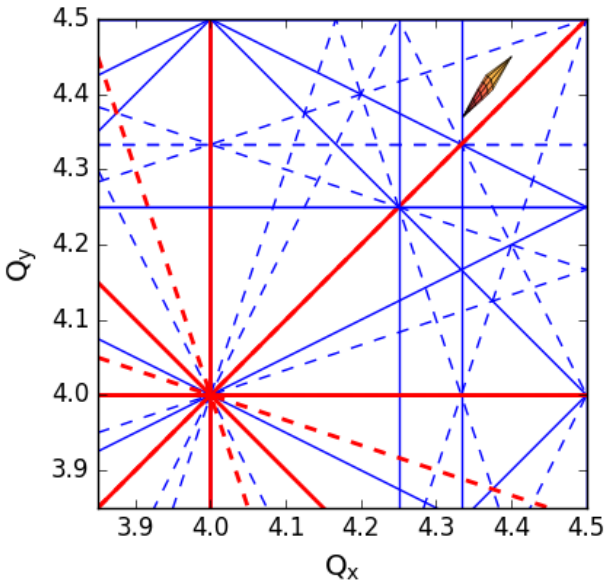

Figure 3.2: Tune spread of the low intensity beam used for the resonance compensation studies.

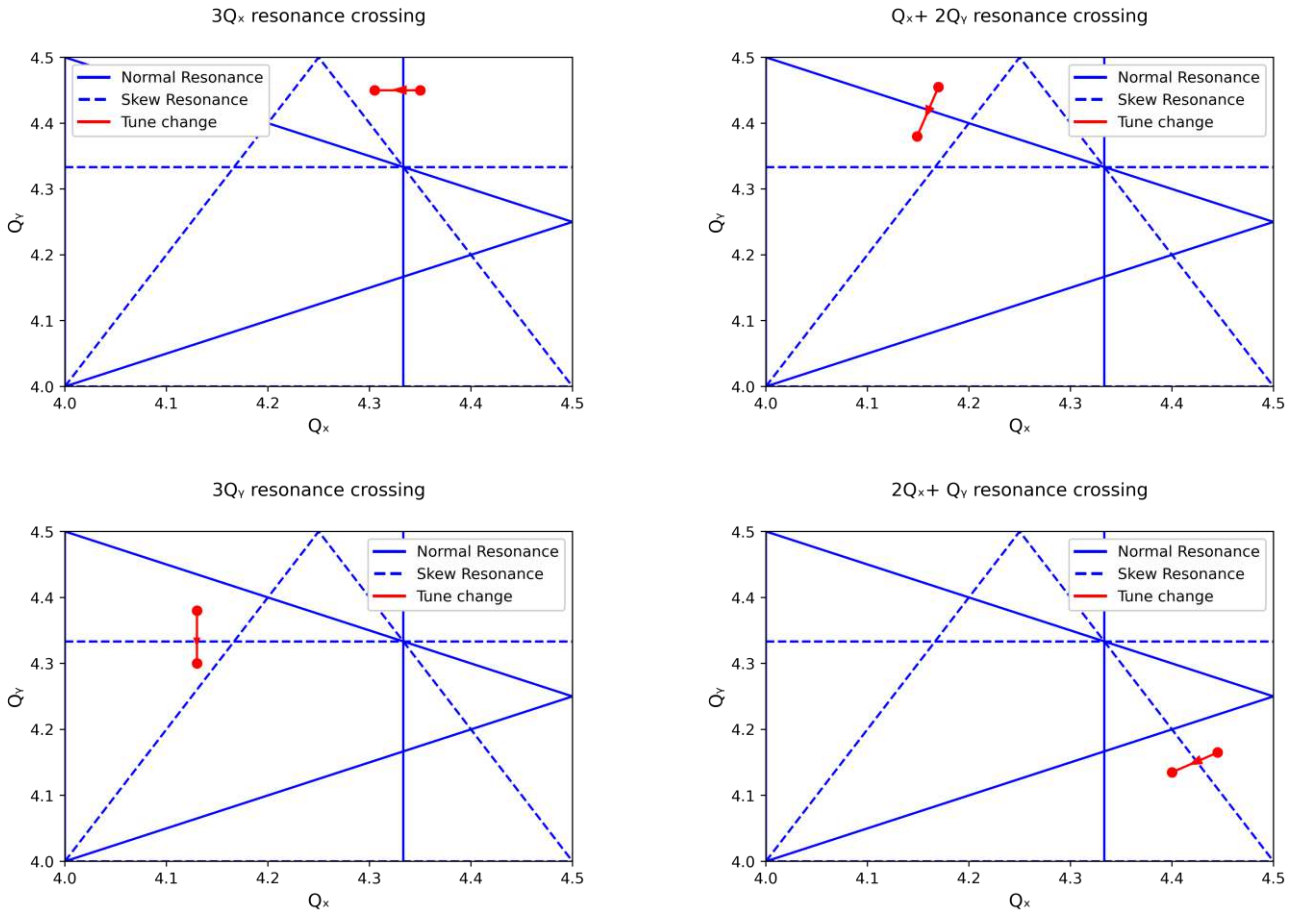

Figure 3.3: Tune changes for the crossings of each of the 3^{rd} order resonances: $3Q_x$ (top left), $Q_x + 2Qy$ (top right), $3Q_y$ (bottom left), $2Q_x + Q_y$ (bottom right).

3.1.1 3^{rd} order normal resonance compensation

Compensating the normal resonances $3Q_x = 13$ and $Q_x + 2Q_y = 13$ requires normal sextupole corrector magnets whose RDTs were calculated using MADX and are represented in Figure 3.4. Two magnets, XNO4L1 and XNO9L1, whose RDTs are perpendicular to each other, were chosen for the individual normal resonance compensation. As the two corrector RDTs are perpendicular, they can be used to cover the entire complex plane of RDTs. Powering these magnets with different currents affects the excitation strength of the resonance which can be observed by monitoring the beam intensity with a beam current transformer (BCT). The losses are then calculated as the relative change in intensity before and after the resonance has been crossed. In a bad configuration, the corrector magnets can thus further enhance the natural resonance excitation strength which increases the losses, which is shown by the red curve in Figure 3.5. The resonance is compensated once these losses are minimized, in which case the intensity, when the resonance is crossed, is represented by the green curve in Figure 3.5. In order to identify the configuration where each resonance is compensated, the currents of both corrector magnets are altered, covering a 2D space of corrector currents, and for each configuration the losses are represented. These losses in terms of the two corrector magnet currents when crossing the $3Q_x$ and the $Q_x + 2Q_y$ resonance in all rings can be seen in Figure 3.6 and Figure 3.7 respectively. The compensating configurations are summarized in Tables 3.1 and 3.2 for both resonances in all rings. Using these currents, the compensating RDTs of both normal resonances in all rings can be represented in a polar plot as in Figure 3.8. This representation is convenient as it can be seen right away which corrector magnets from 3.4 will enhance or reduce resonance excitation if their strength is varied.

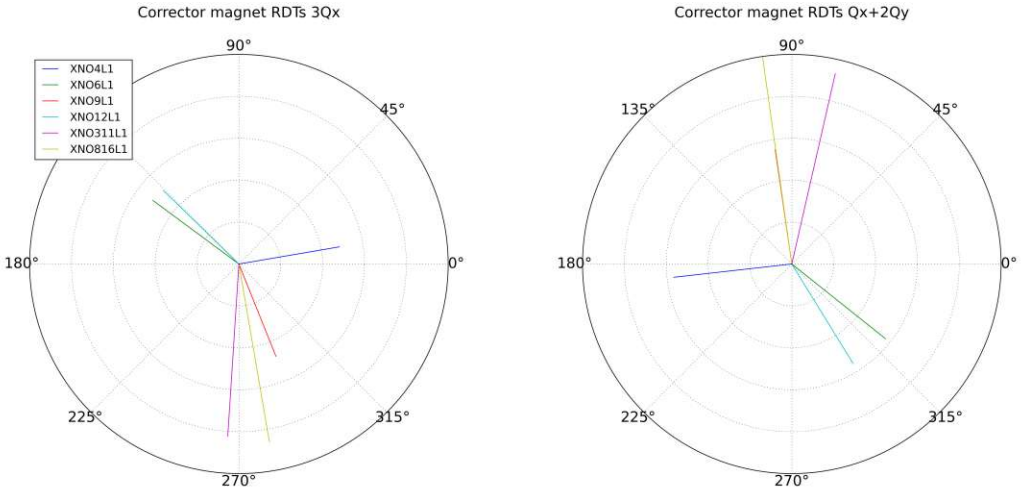

Figure 3.4: Normal sextupole corrector RDTs for the $3Q_x$ resonance(left) and the $Q_x + 2Qy$ resonance(right).

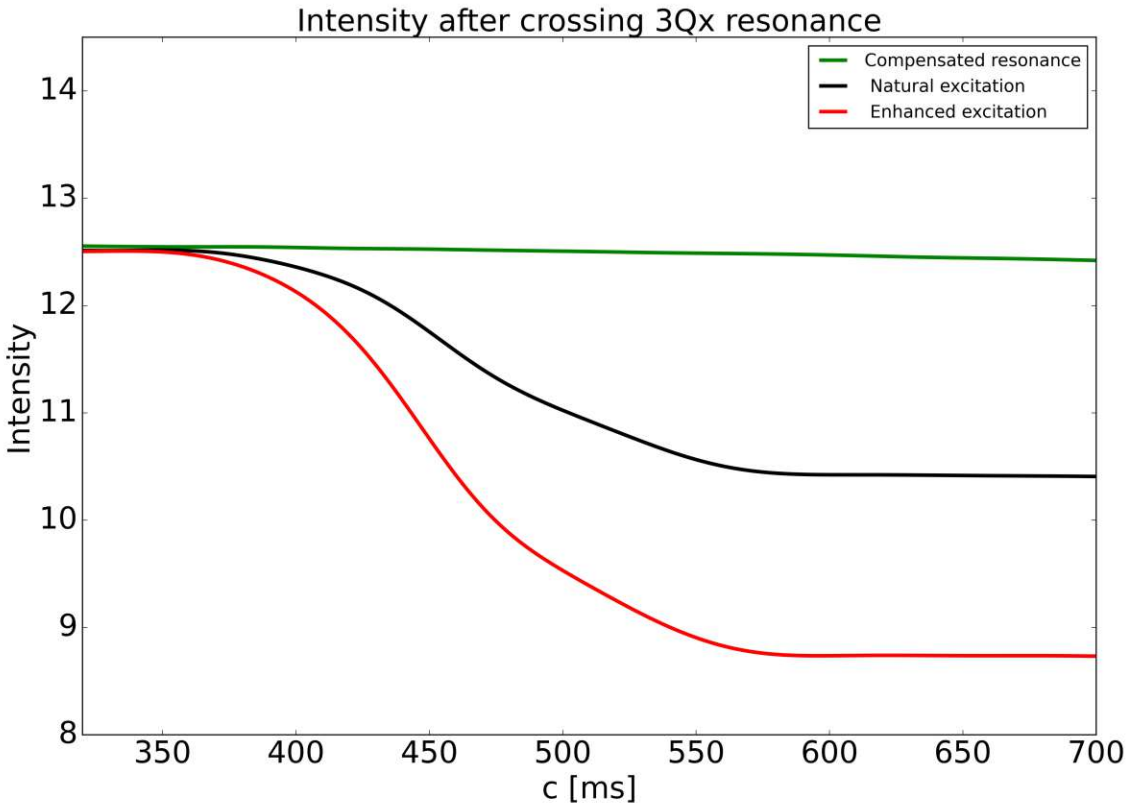

Figure 3.5: Beam intensity during the cycle while crossing the $3Qx$ resonance without any corrector magnets(black), with the corrector magnets in a configuration that further excites the resonance(red) and in the compensating configuration(green).

In order to compare the recently identified compensating configurations with previous studies on resonance compensation, Tables 3.1 and 3.2 also contain the configurations from 2021 and 2018. The latter was before the LHC Injector Upgrade (LIU)[28], which involved major changes in the accelerator complex and increased the brightness of PSB beams by a factor of two[29]. Due to LIU, the changes in the PSB between 2018 and 2021 were significant while only minor changes in the PSB have been made since 2021. This is in line with the observation that the compensation settings seem generally closer to the settings from 2021 than the ones from 2018. Prior to 2021, the normal resonances have not been observed in all rings which is why for some rings there are no values from 2018.

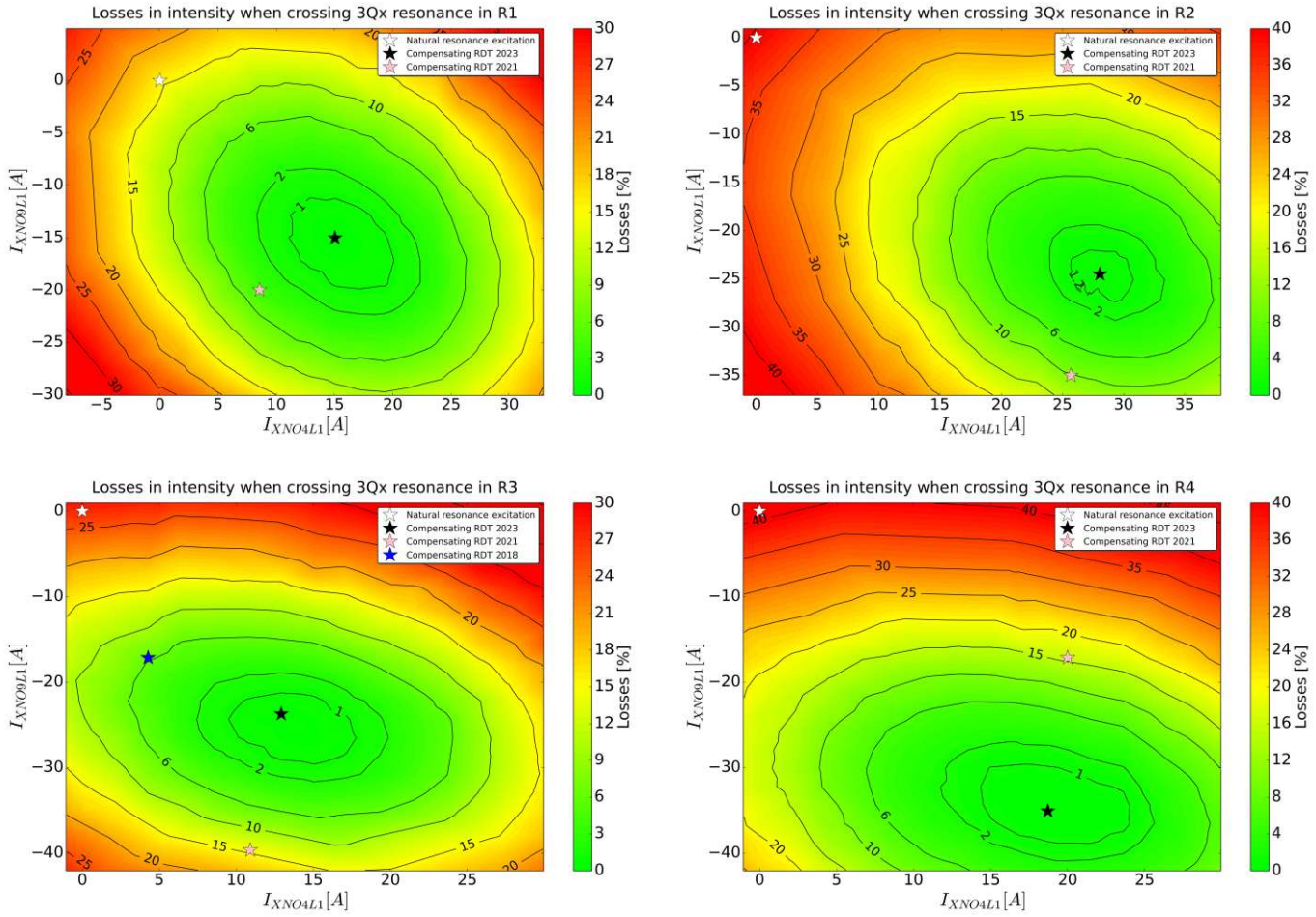

Figure 3.6: Losses when crossing the $3Q_x$ resonance in all rings with different current configurations, the compensating configuration from 2023 is marked by the black star, the pink and blue stars represent the configurations from 2021[30] and 2018[22] respectively. The corresponding configurations can be found in Table 3.1.

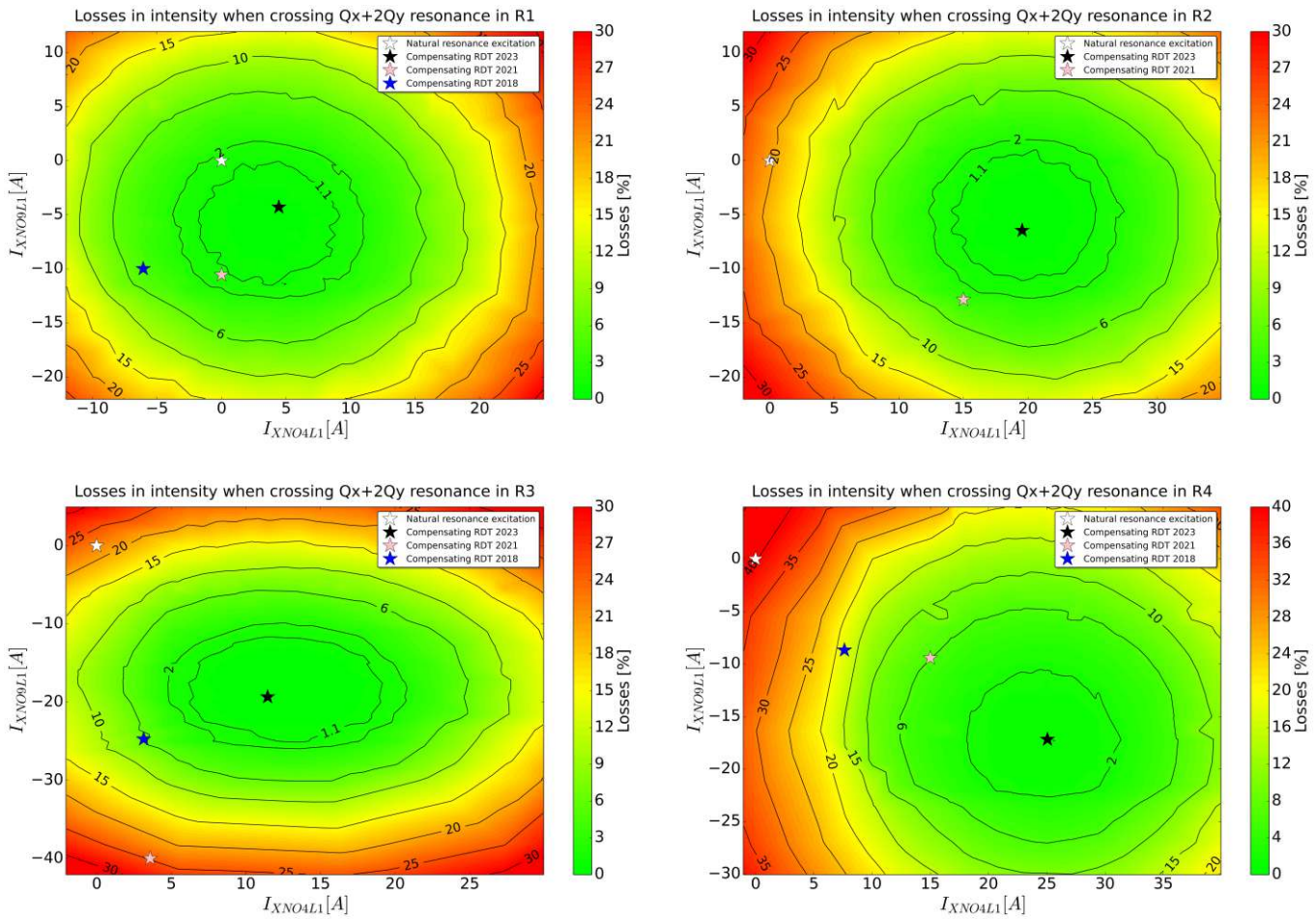

Figure 3.7: Losses when crossing the $Q_x + 2Q_y$ resonance in all rings with different current configurations, the compensating configuration from 2023 is marked by the black star, the pink and blue stars represent the configurations from 2021[30] and 2018[22] respectively. The corresponding configurations can be found in Table 3.2.

3Qx	2023	2021	2018
Ring 4	XNO4L1 = 18.71 A	XNO4L1 = 20 A	n.a.
	XNO9L1 = -35.09 A	XNO9L1 = -17.14 A	n.a.
Ring 3	XNO4L1 = 12.92 A	XNO4L1 = 10.9 A	XNO4L1 = 4.28 A
	XNO9L1 = -23.72 A	XNO9L1 = -39.64 A	XNO9L1 = -17.14 A
Ring 2	XNO4L1 = 28.07 A	XNO4L1 = 25.7 A	n.a.
	XNO9L1 = -24.50 A	XNO9L1 = -34.99 A	n.a.
Ring 1	XNO4L1 = 15.04 A	XNO4L1 = 8.57 A	n.a.
	XNO9L1 = -15.04 A	XNO9L1 = -20A	n.a.

Table 3.1: Normal sextupole corrector current configurations for the compensation of the $3Q_x$ resonance from 2023, from 2021[30] and from 2018[22].

Qx+2Qy	2023	2021	2018
Ring 4	XNO4L1 = 25.06 A	XNO4L1 = 15 A	XNO4L1 =7.63 A
	XNO9L1 = -17.18 A	XNO9L1 = -9.44 A	XNO9L1 = -8.68 A
Ring 3	XNO4L1 = 11.46 A	XNO4L1 = 3.58 A	XNO4L1 =3.15 A
	XNO9L1 = -19.33 A	XNO9L1 = -39.99 A	XNO9L1 = -24.73 A
Ring 2	XNO4L1 = 19.55 A	XNO4L1 = 15 A	n.a.
	XNO9L1 = -6.44 A	XNO9L1 = -12.85 A	n.a.
Ring 1	XNO4L1 = 4.44 A	XNO4L1 = 0 A	XNO4L1 = -6.07 A
	XNO9L1 = -4.30 A	XNO9L1 = -10.56A	XNO9L1 = - 9.99 A

Table 3.2: Normal sextupole corrector current configurations for the compensation of the $Q_x + 2Q_y$ resonance from 2023, from 2021[30] and from 2018[22].

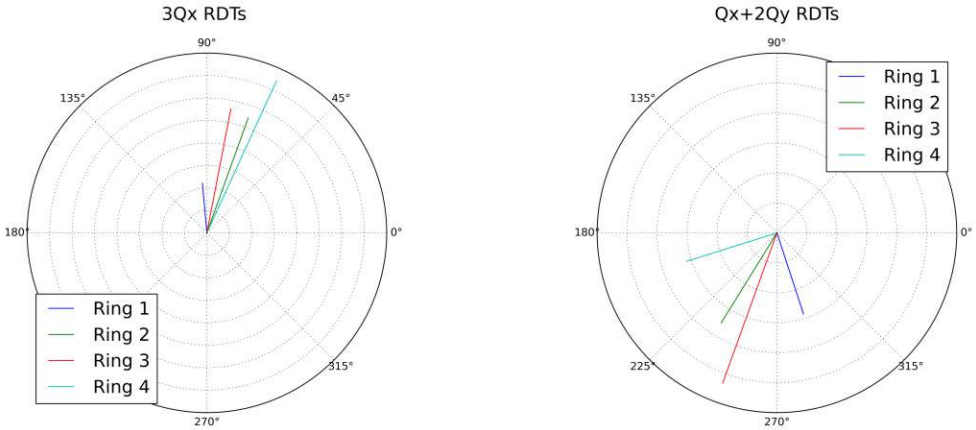

Figure 3.8: Compensating RDTs for both normal 3$^{\text{rd}}$ order resonances in all rings represented in a polar plot.

Effect of chromaticity correction on normal 3^{rd} order resonances

In the PSB, chromaticity can be controlled with sextupoles installed in each cell (harmonic sextupoles). As these magnets are connected in series, the chromaticity can not be compensated in both planes at the same time. This configuration of the harmonic sextupoles should only drive systematic 3^{rd} order resonances, allowing for chromaticity corection without exciting the non-systematic 3^{rd} order resonances in the operational tune regime, as their individual contributions will cancel out due to the periodicity[10]. However, their impact on the excited resonances has to be evaluated as any differences between the magnets can lead to non-perfect cancellation, which breaks the periodicity of the machine and drives non-systematic resonances. The normal 3^{rd} order resonances were crossed with the harmonic sextupoles set to correct horizontal chromaticity as well as vertical chromaticity. The losses for different corrector strengths while correcting chromaticity in each plane can be seen in Figure 3.9 and Figure 3.10. As can be seen in these figures, chromaticity correction affects both non-systematic 3^{rd} order normal resonances differently in all rings. Vertical chromaticity correction does not significantly affect the $3Q_x$ resonance compensation settings in rings 1 and 3 with the losses being at less than 1% with and without chromaticity correction. Horizontal chromaticity correction however in ring 2 changes $3Q_x$ resonance compensation significantly with the losses being around 10% if chromaticity correction is not taken into account. Chromaticity correction in either plane affects the $Q_x + 2Q_y$ resonance more significantly than the $3Q_x$ resonance in all rings.

For an operational cycle where chromaticity has to be corrected, it is thus important to take into account how harmonic sextupoles affect non-systematic 3^{rd} order resonances. It was also observed that harmonic sextupoles affect skew resonances. However, no full dataset was collected to further explore how skew resonance compensation changes specifically due to harmonic sextupoles.

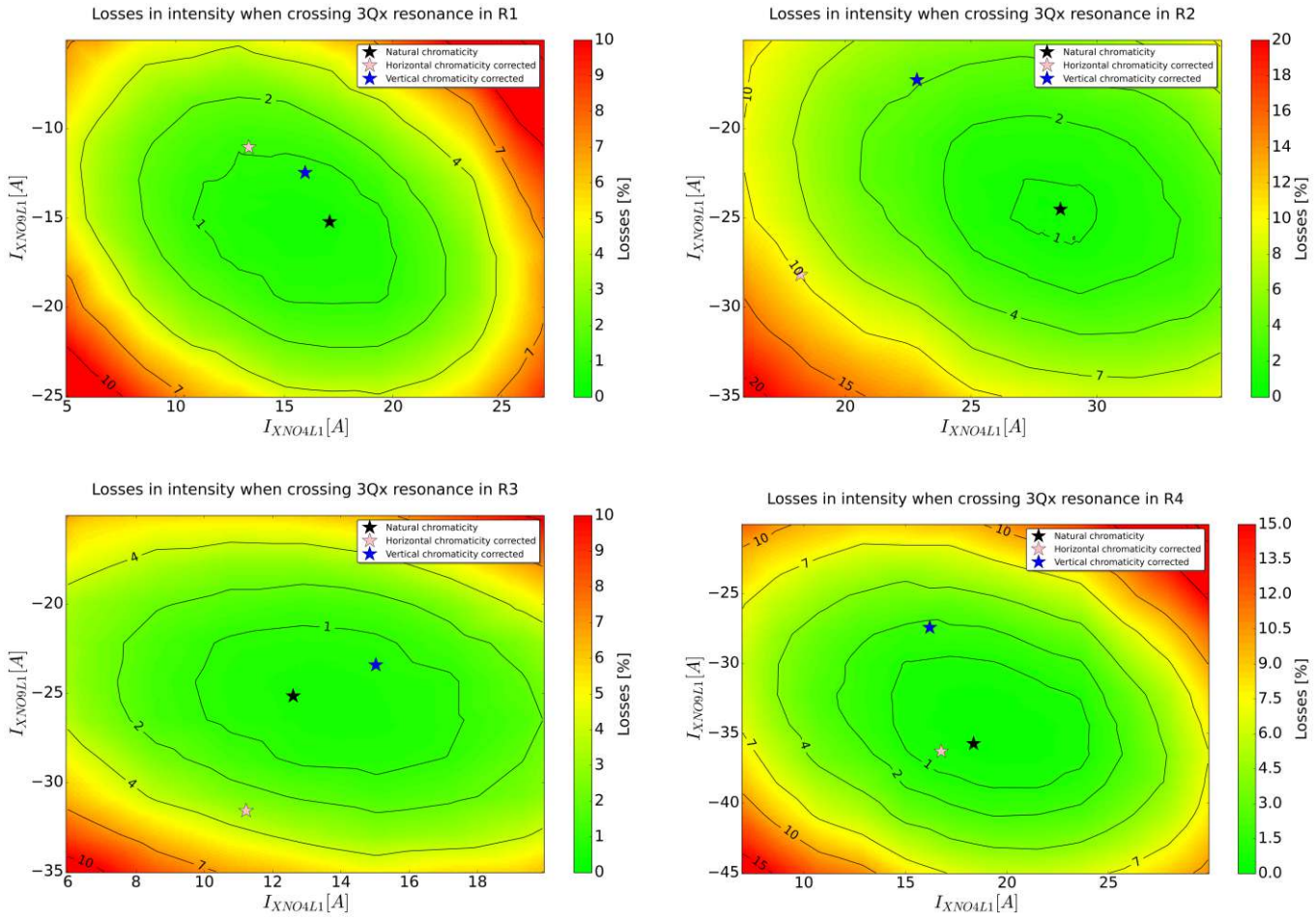

Figure 3.9: Losses when crossing the $3Q_x$ resonance in all rings with different current configurations. The black star shows the natural chromaticity and pink and blue the corrected chromaticity in the horizontal and vertical plane respectively.

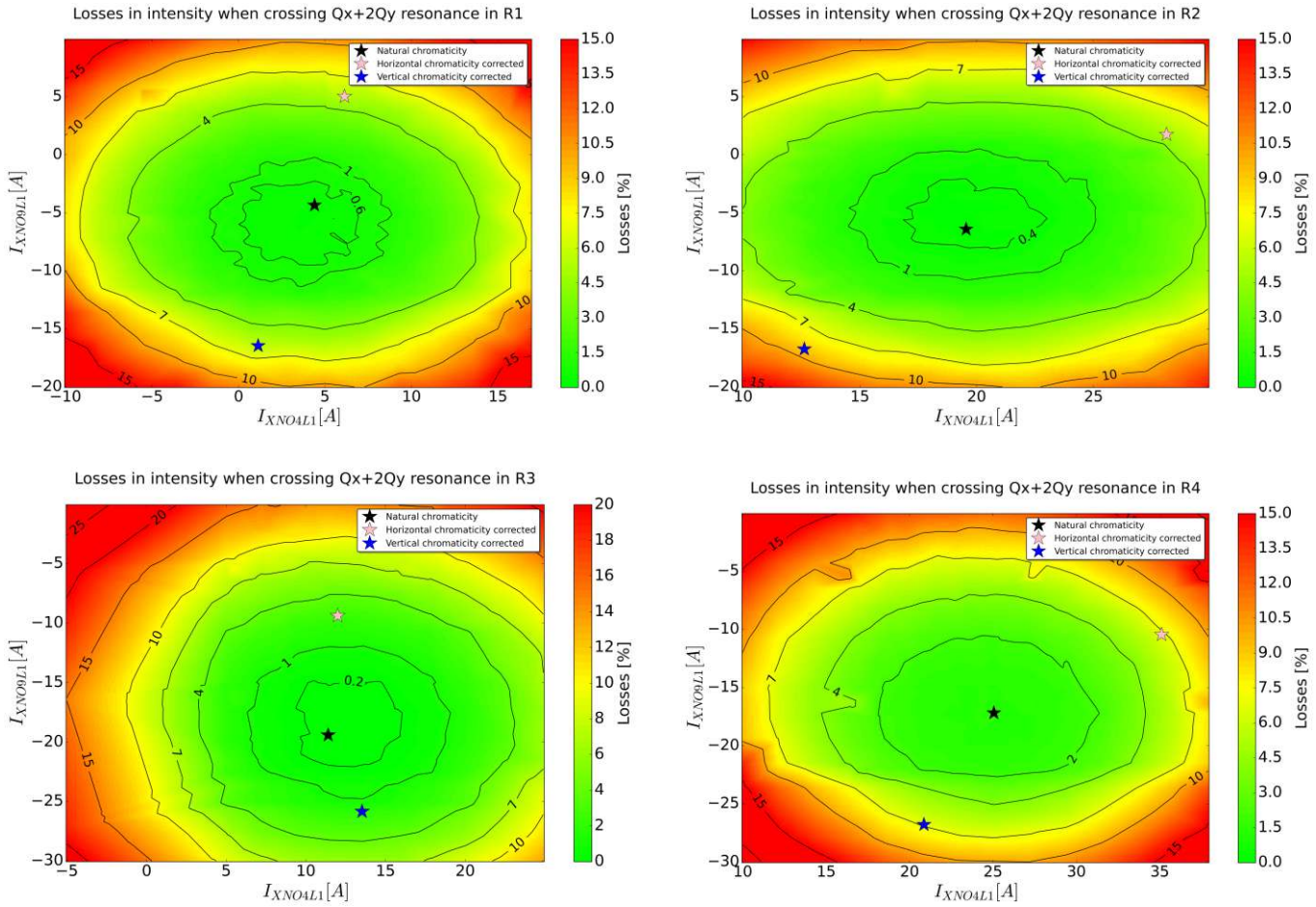

Figure 3.10: Losses when crossing the $Q_x + 2Q_y$ resonance in all rings with different current configurations. The black star shows the natural chromaticity and pink and blue the corrected chromaticity in the horizontal and vertical plane respectively.

3.1.2 3^{rd} order skew resonance compensation

The 3^{rd} order skew resonances that will be individually compensated are $3Q_y = 13$ and $2Q_x + Qy = 13$. These are driven by skew sextupole-like magnet errors and they can be compensated using skew sextupoles. Similar to the normal sextupoles, the RDTs of the skew corrector magnets were calculated and plotted in Figure 3.11.

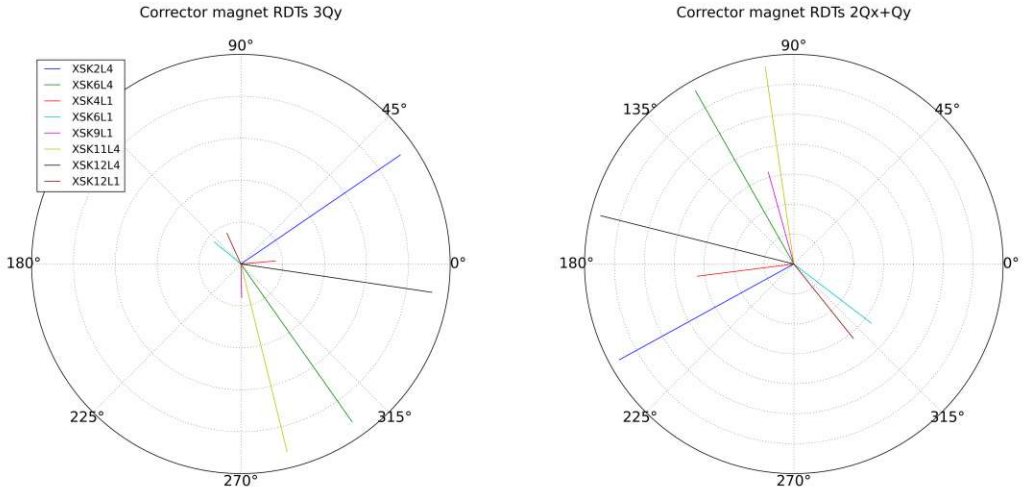

Figure 3.11: Skew sextupole corrector RDTs for the $3Q_y$ resonance (left) and the $2Q_x + Qy$ resonance (right).

While there are more skew sextupole corrector magnets installed, only three of them are equipped with a power supply, namely XSK2L4, XSK4L1 and XSK6L4. The two correctors whose RDTs are orthogonal and suitable for compensating the skew resonances are XSK2L4 and XSK6L4. The procedure that was followed is similar to the case of normal resonance compensation. Each of the skew resonances were crossed individually in all rings with varied corrector magnet strengths in order to identify the compensating configuration. The losses when crossing the $3Q_y$ resonance with different corrector magnet currents are plotted in Figure 3.12 with the corresponding compensating current configurations in Table 3.3.

In ring 1, the $3Q_y$ resonance has been compensated in a study on resonance compensation from 2004[23]. In this study however, the injection energy of the protons was 50MeV and vertical chromaticity was corrected to zero, thus the experimental circumstances of resonance compensation have been different. Another magnet has been used for the compensation in 2004, however the compensating RDT can be expressed in terms of the magnets used in the current study and represented in the same plot in Figure 3.12. Given the changes in injection energy, in chromaticity correction settings and in the magnet lattice in the last two decades, this comparison shows that the resonance has not changed that significantly. Further, the losses with natural resonance excitation have remained the same over the last two decades, around 20%, indicating that the natural resonance excitation remained the same.

In ring 2, no losses were observed when crossing the $3Q_y$ resonance in 2004, thus compensation was not necessary.

For the $2Q_x + Q_y$ resonance, the losses with different corrector magnet currents are plotted in Figure 3.13 with the compensating currents in Table 3.4. The compensating skew RDTs for both resonances in all rings are shown in a polar plot in Figure 3.14.

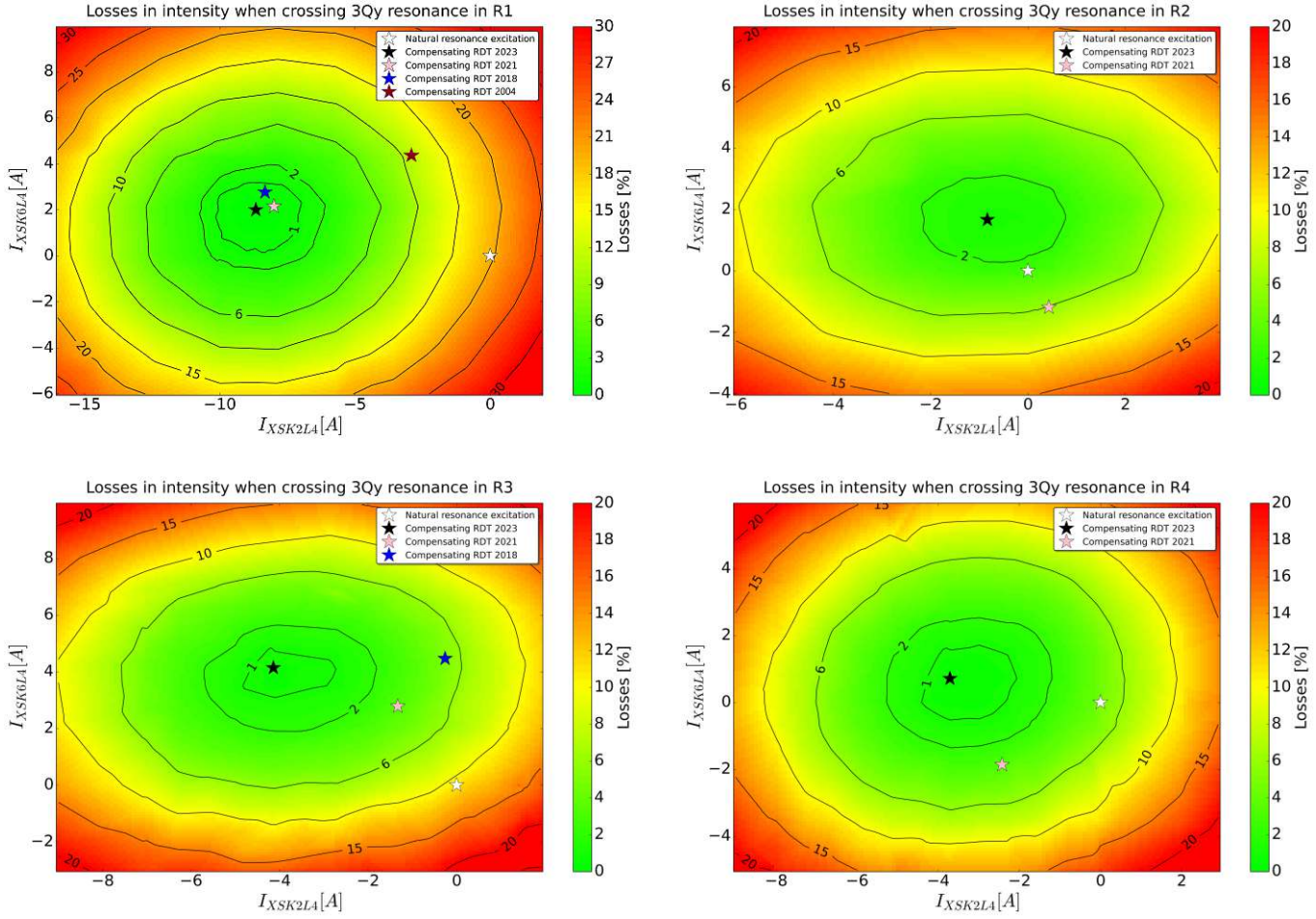

Figure 3.12: Losses when crossing the $3Q_y$ resonance in all rings with different current configurations, the compensating configuration from 2023 is marked by the black star, the pink and blue stars represent the configurations from 2021[30] and 2018[22] respectively. The corresponding configurations can be found in Table 3.3.

3Qy	2023	2021	2018	2004
R4	XSK2L4 = -3.71 A XSK6L4 = 0.71 A	XSK2L4 = -2.43 A XSK6L4 = -1.86 A	n.a. n.a.	
R3	XSK2L4 = -4.14 A XSK6L4 = 4.14 A	XSK2L4 = -1.33 A XSK6L4 = 2.78 A	XSK2L4 = -0.26 A XSK6L4 = 4.47 A	
R2	XSK2L4 = -0.83 A XSK6L4 = 1.67 A	XSK2L4 = 0.43 A XSK6L4 = -1.19 A	n.a. n.a.	
R1	XSK2L4 = -8.674 A XSK6L4 = 2.0 A	XSK2L4 = -8 A XSK6L4 = 2.15A	XSK2L4 = -8.33 A XSK6L4 = 2.77 A	XSK9L1 = 31 A

Table 3.3: Skew sextupole corrector current configurations for the compensation of the $3Q_y$ resonance from 2023, from 2021[30] and from 2018[22]. In ring 1, the resonance was compensated already in 2004[23].

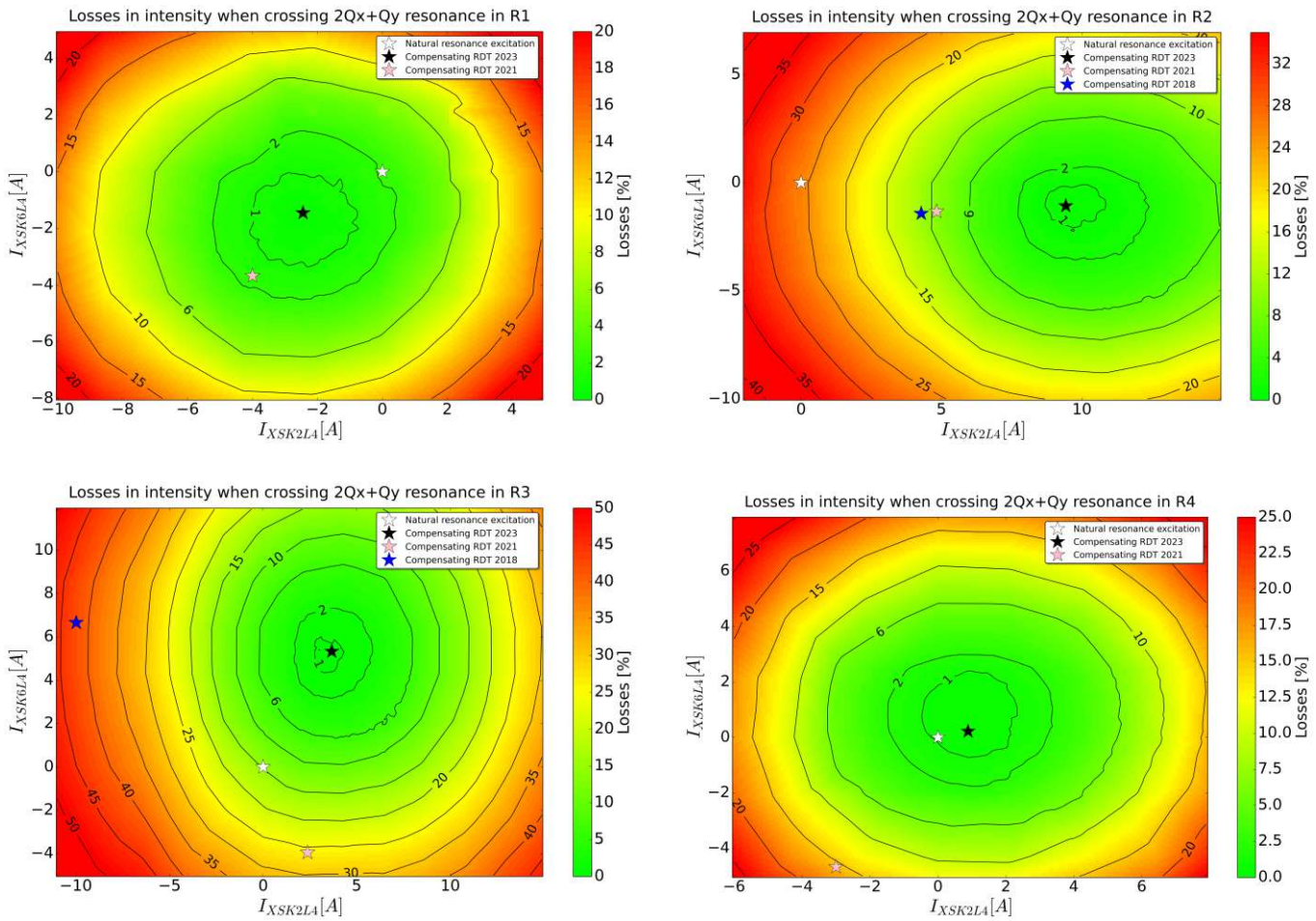

Figure 3.13: Losses when crossing the $2Q_x + Q_y$ resonance in all rings with different current configurations, the compensating configuration from 2023 is marked by the black star, the pink and blue stars represent the configurations from 2021[30] and 2018[22] respectively. The corresponding configurations can be found in Table 3.4.

2Qx+Qy	2023	2021	2018
R4	XSK2L4 = 0.89 A XSK6L4 = 0.78 A	XSK2L4 = -3 A XSK6L4 = -4.67 A	n.a. n.a.
R3	XSK2L4 = 3.67 A XSK6L4 = 5.33 A	XSK2L4 = 2.37 A XSK6L4 = -3.95 A	XSK2L4 = -9.99 A XSK6L4 = 6.66 A
R2	XSK2L4 = 9.11 A XSK6L4 = -0.56 A	XSK2L4 = 4.83 A XSK6L4 = -1.33 A	XSK2L4 = 4.28 A XSK6L4 = -1.42 A
R1	XSK2L4 = -1.89 A XSK6L4 = -2.0 A	XSK2L4 = -4 A XSK6L4 = -3.67 A	n.a. n.a.

Table 3.4: Skew sextupole corrector current configurations for the compensation of the $2Q_x + Q_y$ resonance from 2023, from 2021[30] and from 2018[22].

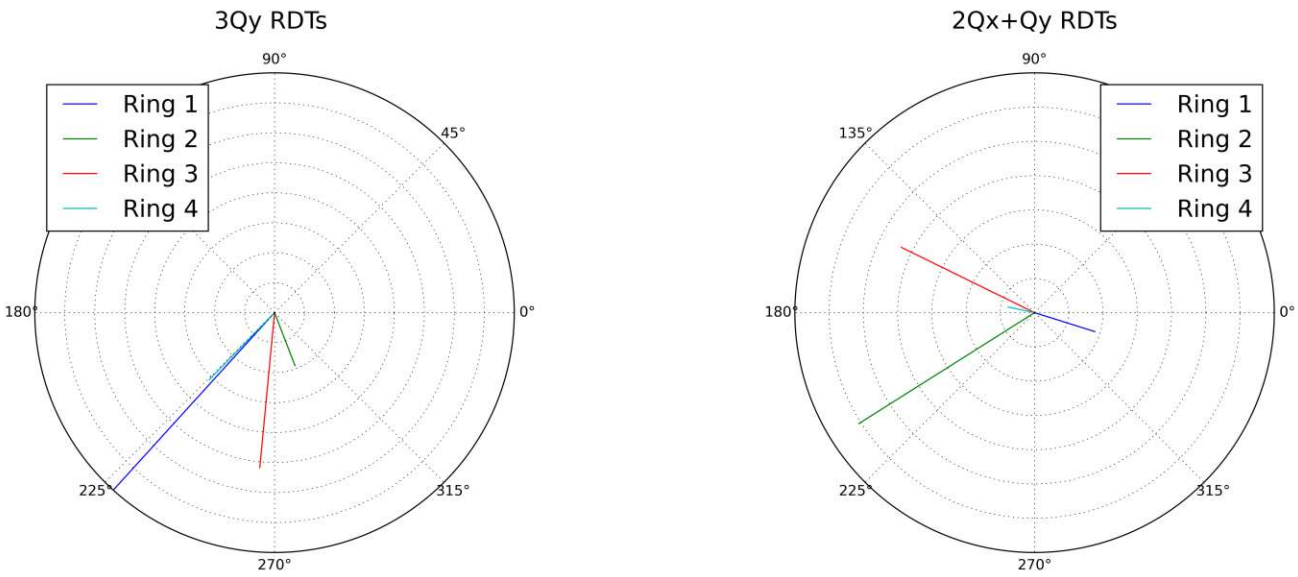

Figure 3.14: Compensating RDTs for both skew resonances represented in a polar plot.

3.1.3 4^{th} order resonance compensation

The normal 4^{th} order resonances $4Q_x$, $2Q_x + 2Q_y$ and $4Q_y$ are excited in all rings and can be compensated using normal octupole magnets [27]. The method for the identification of the compensating RDT is the same as for the 3^{rd} order resonances. The RDTs of the normal octupole corrector magnets for the same normalized magnet strength were calculated using PTC in MADX and are represented in Figure 3.15.

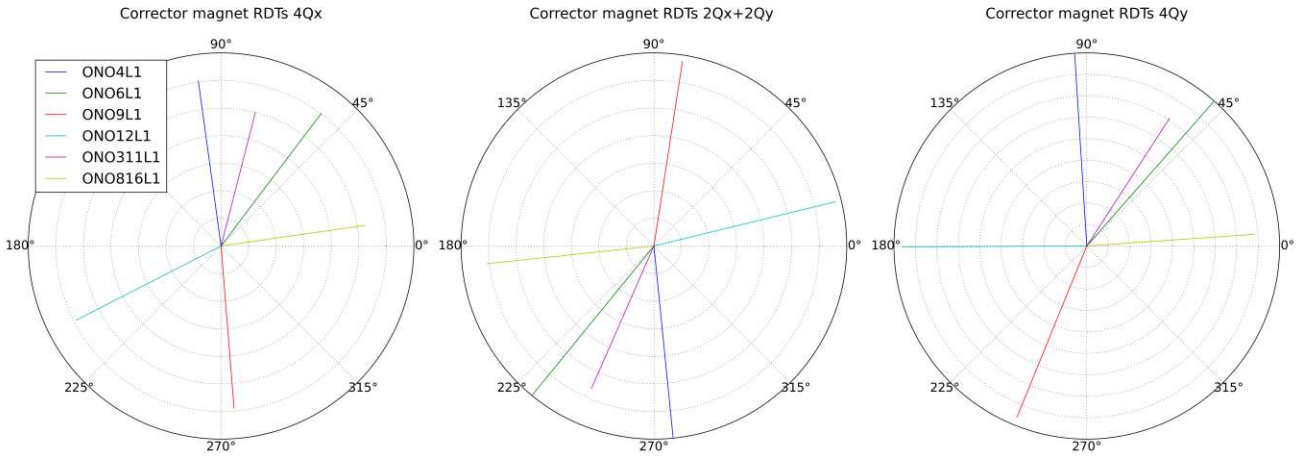

Figure 3.15: Octupole Corrector RDTs for the $4Q_x$ resonance on the left, the $2Q_x + 2Q_y$ resonance in the middle and the $4Q_y$ resonance on the right.

The octupoles used for 4^{th} order resonances are ONO311L1 and ONO816L1. The current configurations that were used to identify the compensating RDTs are depicted in Figure 3.16. It can be seen that even at the highest allowed currents, only partial resonance compensation was achieved. Further, as this partial resonance compensation was found with a flat bottom cycle at injection energy, the degree of compensation will further deteriorate as particles are accelerated. As the magnetic field is ramped up, the corrector magnet currents have to be increased accordingly to keep up the compensation, which is not possible due to the currents already being at their limits. During this study it was also observed that the ONO311L1 was connected with the opposite polarity with respect to the MADX model, leading to an inconsistency with the calculated RDT.

In order to overcome the current limitations and achieve full resonance compensation, more octupoles were combined to extended knobs whose effective currents are doubled. Using corrector magnets whose RDTs are rotated by 180° and powered with opposite currents, they can be combined into a stronger knob. The first knob was made up of ONO9L1 and ONO4L1(with a negative current) and the second knob was made up of ONO816L1 and ONO12L1(with a negative current). Using these extended knobs, full compensation could be achieved in all rings as can be seen in Figure 3.17. Further, compensating 4^{th} order resonances with the extended knobs requires less currents per magnet, allowing for the compensation to be kept up for as long as necessary while the magnetic field ramps up throughout the cycle. The compensating RDTs were calculated using MADX and plotted in polar plots in Figure 3.18. As it has been observed previously[5], the settings for the compensation of all three 4^{th} order normal resonances are identical and achieve global resonance compensation. Further,

the RDTs of each resonance look very similar in each of the rings. This would indicate that a single localized octupole-like error drives all of the 4^{th} order resonances.

In the past, the Generic Optimisation Frontend and Framework (GeOFF) [31–34] has been used to identify the octupole compensation settings. The settings found with this optimisation algorithm are in agreement with the ones found using the extended knobs, as can be seen in Figure 3.18.

The corresponding settings that have been identified using the initial and extended pair of magnets along with the optimizer are summarized in Table 3.5.

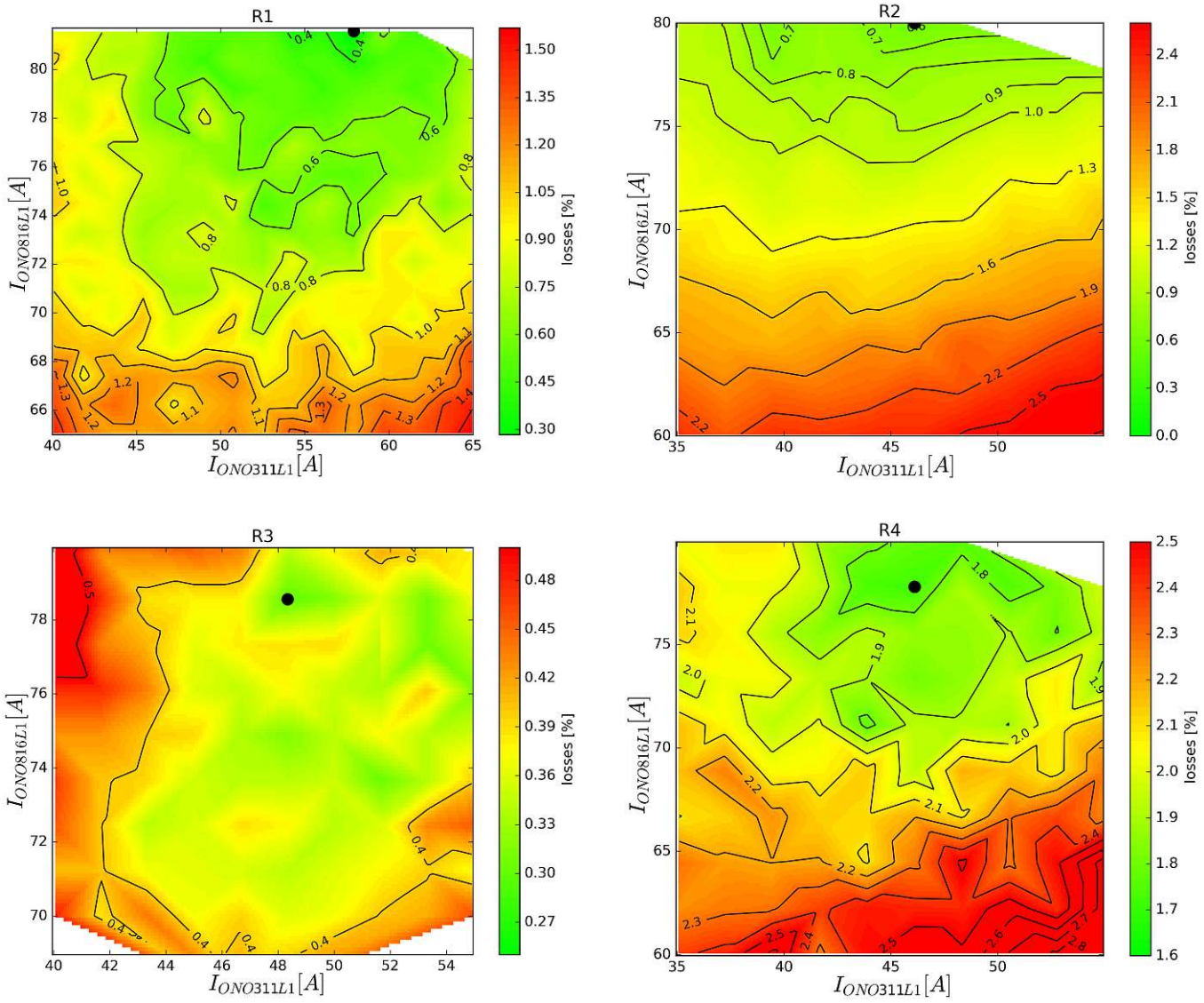

Figure 3.16: Losses when crossing the 4^{th} order resonance in all rings using a pair of octupoles in different current configurations.

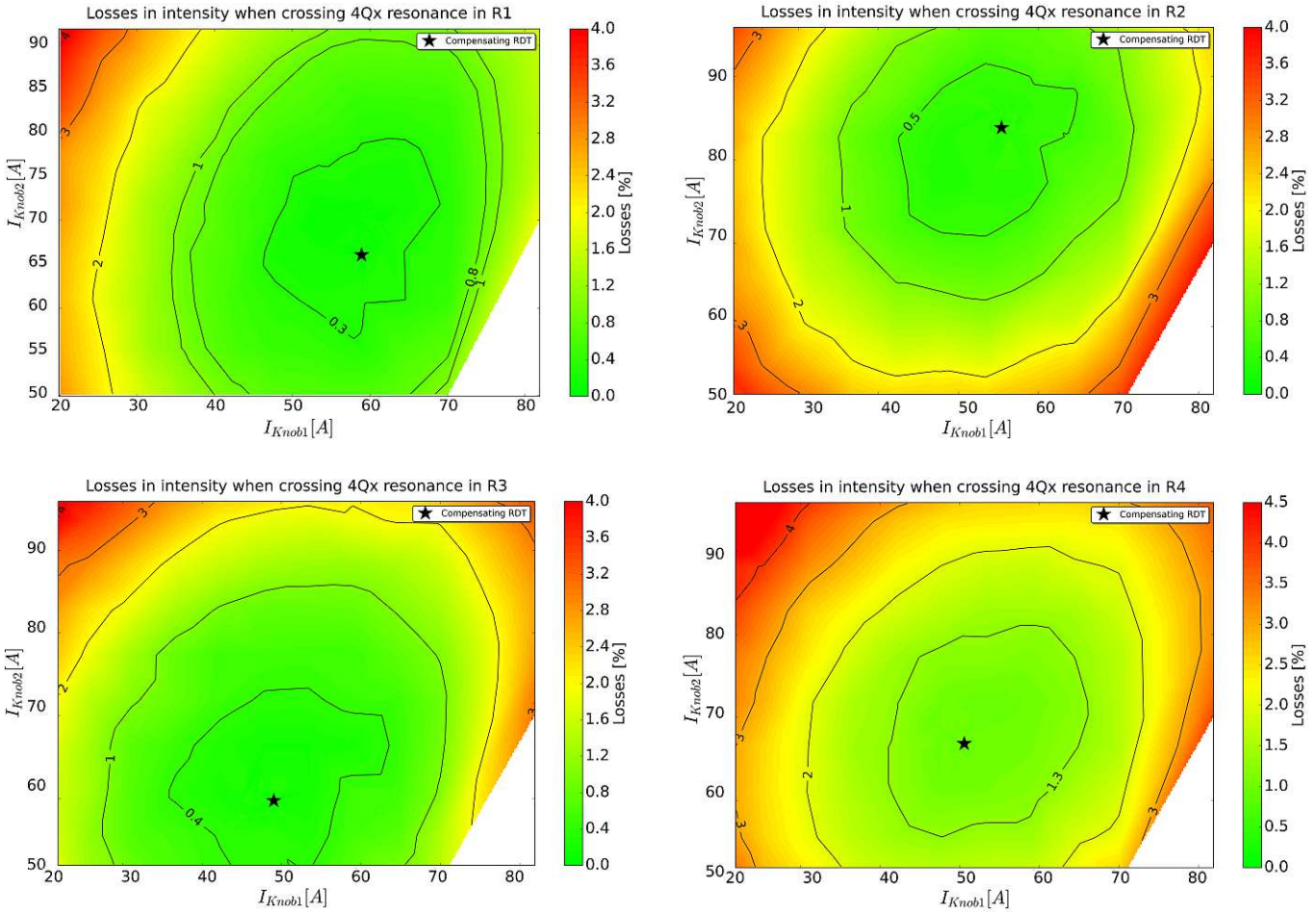

Figure 3.17: Losses when crossing the 4^{th} order resonance in all rings using the two extended knobs in different current configurations.

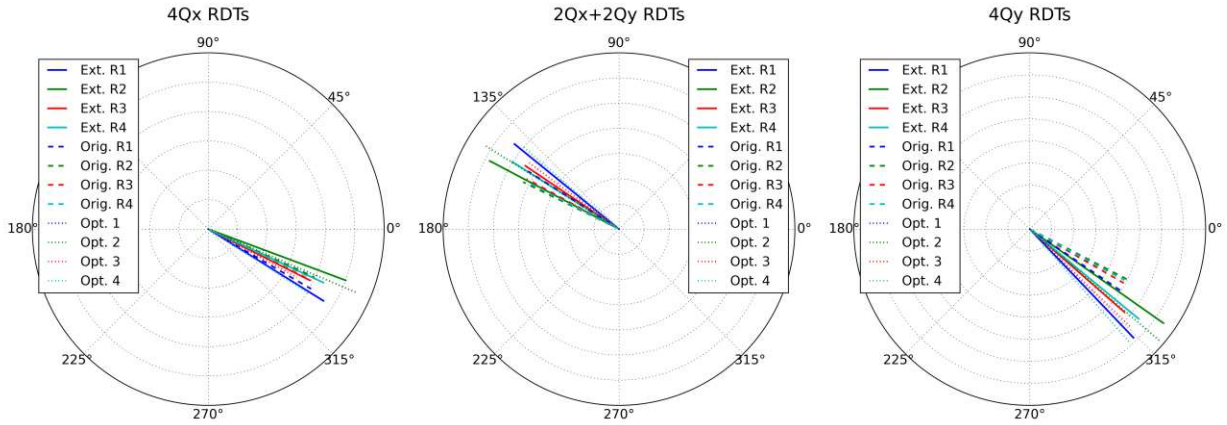

Figure 3.18: Compensating RDTs for the $4Q_x$ resonance on the left, the $2Q_x + 2Q_y$ resonance in the middle and the $4Q_y$ resonance on the right. The compensating configurations using the original knobs(dashed lines), the extended knobs(solid lines) and the optimizer algorithm(dotted lines) in all rings were taken from Table 3.5.

Rings	Extended knobs	Original Knobs	Optimizer
Ring 1	ONO4L1 = -30.35 A ONO9L1 = 30.35 A ONO12L1 = -33.69 A ONO816L1 = 33.69 A	ONO311L1 = 57.9 A ONO816L1 = 81.57 A	ONO4L1 = -49.9 A ONO6L1 = 49.9 A ONO9L1 = 49.9 A ONO12L1 = -49.9 A
Ring 2	ONO4L1 = -26.69 A ONO9L1 = 26.69 A ONO12L1 = -41.36 A ONO816L1 = 41.36 A	ONO311L1 = 46.11 A ONO816L1 = 80 A	ONO4L1 = -49.9 A ONO6L1 = 49.9 A ONO9L1 = 49.9 A ONO12L1 = -49.9 A
Ring 3	ONO4L1 = -23.4 A ONO9L1 = 23.4 A ONO12L1 = -30.08 A ONO816L1 = 30.08 A	ONO311L1 = 48.33 A ONO816L1 = 78.55 A	ONO4L1 = -49.9 A ONO12L1 = -49.7 A
Ring 4	ONO4L1 = -25.29 A ONO9L1 = 25.29 A ONO12L1 = -34.3 A ONO816L1 = 34.3 A	ONO311L1 = 46.11 A ONO816L1 = 77.78 A	ONO4L1 = -49.9 A ONO6L1 = 11.8 A ONO9L1 = 18.8 A ONO12L1 = -48.4 A

Table 3.5: Different octupole configurations that compensate the normal 4^{th} order resonances. The original magnets that were limited by currents were replaced by the extended knobs to determine the compensating RDT. The compensating configuration found by the optimizer algorithm is also limited by the maximum current of 50 A.

3.1.4 Effect of the 4^{th} order resonance compensation on 3^{rd} order resonances

It was observed in previous studies that 4^{th} order resonance compensation affects 3^{rd} order resonances [5]. Individual resonance compensation of 3^{rd} order resonances is still possible with octupoles correctors on and the altered compensation settings are given in Table 3.7 and 3.8. An effort was made to further investigate how octupoles drive 3^{rd} order resonances. As magnet misalignments such as displacements or rotations of magnets cause lower-order feed-down fields, misaligned octupoles induce additional sextupolar fields which affect 3^{rd} order resonances[12]. In order to estimate this effect, octupole misalignments in the machine have been measured and were added in the magnet lattice in MADX to calculate the effect of the octupole feed-down fields on 3^{rd} order resonances. The calculated 3^{rd} order RDTs with the misaligned octupoles were added in Figures 3.25 to 3.28, from which it is apparent that the estimated RDTs were not consistent with the measured ones.

Compensation of the $Q_x + 2Q_y$ resonance has been tested with different sets of octupole correctors that produce the same RDT and all compensate the 4^{th} order resonances as shown in Figure 3.19. However, it was observed that when using specific octupole correctors, no compensating settings were found for the normal $Q_x + 2Q_y$ resonance. The loss pattern with different octupoles depicted in Figure 3.20 points to a splitting of the resonance. This effect is not yet understood and more studies are needed.

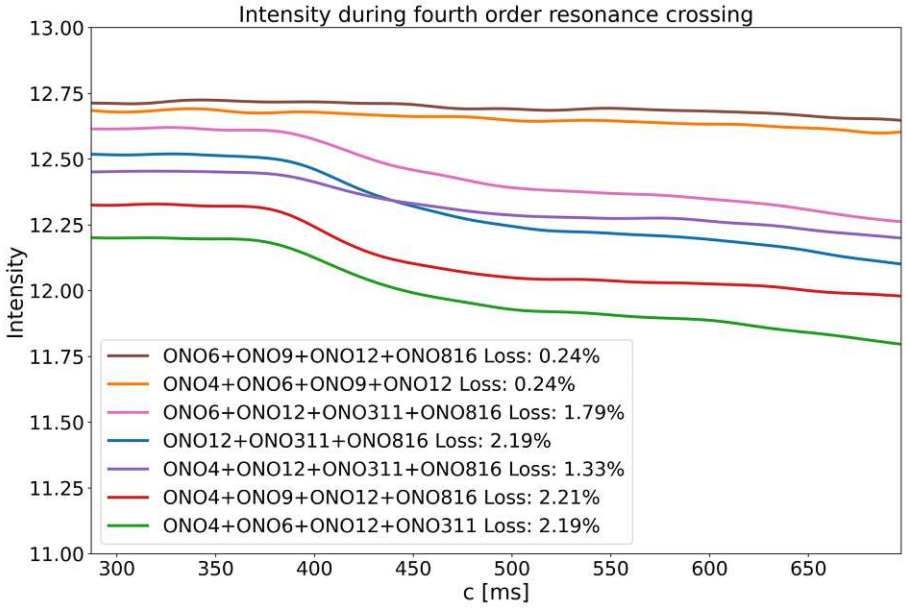

Figure 3.19: Intensity curves when crossing all normal 4^{th} order resonances in ring 4 using different sets of octupole correctors magnets that all compensate the resonances. The remaining losses are due to limitations in current for some of the corrector magnets.

As it turns out, $Q_x + 2Q_y$ resonance is not possible with the octupoles that were used for the extended knobs in the previous section. Thus in order to compensate all 3^{rd} and 4^{th} order resonances simultaneously, only the set of octupoles that do not disturb $Q_x + 2Q_y$ resonance compensation can be used. From this reduced set of octupoles, the best configuration that fully compensates 4^{th} order resonances was found and is shown for all rings in Table 3.6.

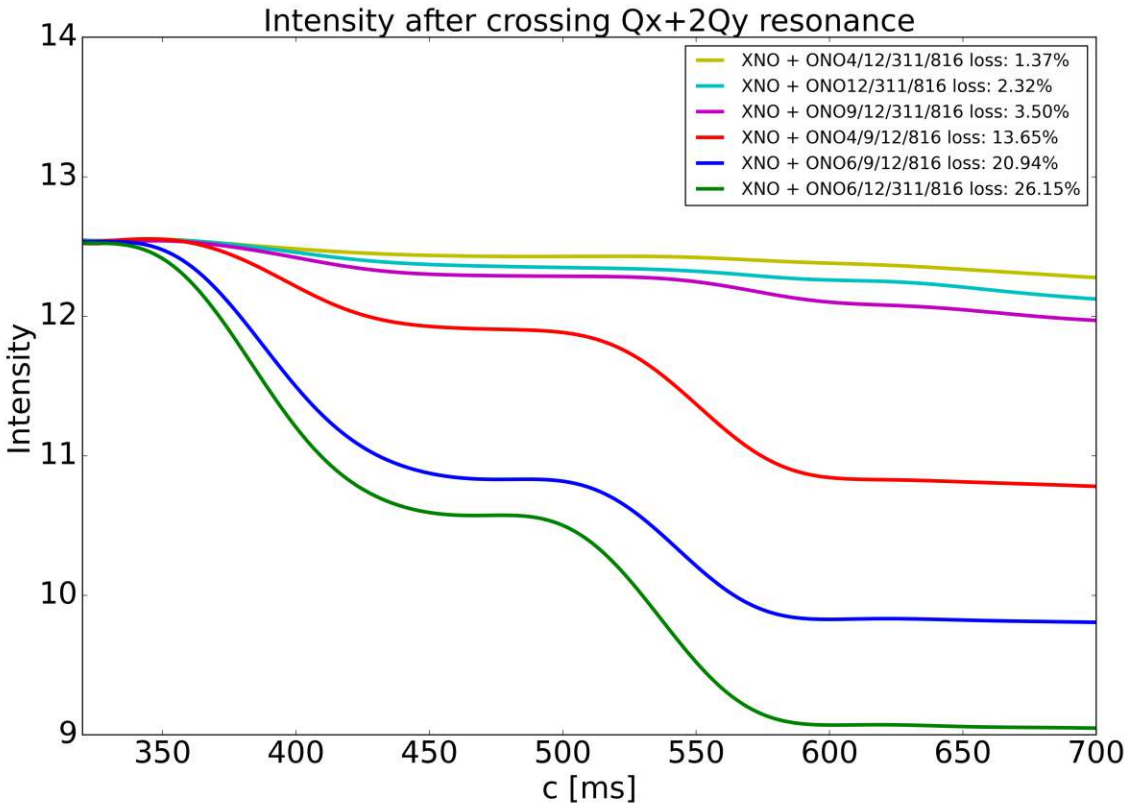

Figure 3.20: Intensity curves when trying to compensate the $Q_x + 2Q_y$ resonance with different octupole correctors on. Sextupole correctors are chosen in a way that the losses are minimized, in three cases (yellow, pink and light blue) the resonance is almost fully compensated. In the other three cases, the losses could not be further reduced and resonance compensation is not possible. In the latter cases, it looks like the $Q_x + 2Q_y$ resonance is split in two, with losses at two different periods of the cycle.

Rings	Extended knobs	Alternative configuration
Ring 1	ONO4L1 = -30.35 A ONO9L1 = 30.35 A ONO12L1 = -33.69 A ONO816L1 = 33.69 A	ONO4L1 = -8.55 A ONO12L1 = -50 A ONO311L1 = 74.7 A ONO816L1 = 40.05 A
Ring 2	ONO4L1 = -26.69 A ONO9L1 = 26.69 A ONO12L1 = -41.36 A ONO816L1 = 41.36 A	ONO4L1 = -7.52 A ONO12L1 = -50 A ONO311L1 = 65.69 A ONO816L1 = 46.95 A
Ring 3	ONO4L1 = -23.4 A ONO9L1 = 23.4 A ONO12L1 = -30.08 A ONO816L1 = 30.08 A	ONO4L1 = -6.6 A ONO12L1 = -43.52 A ONO311L1 = 57.59 A ONO816L1 = 34.97 A
Ring 4	ONO4L1 = -25.29 A ONO9L1 = 25.29 A ONO12L1 = -34.3 A ONO816L1 = 34.3 A	ONO4L1 = -7.13 A ONO12L1 = -48.82 A ONO311L1 = 62.24 A ONO816L1 = 39.59 A

Table 3.6: Different octupole configurations that compensate fourth order resonances globally. The extended knobs have been used to initially determine the compensating RDT and one of the possible alternative configurations is given on the right.

Qx+2Qy	XNO+OCT	3Qx	XNO+OCT
Ring 4	XNO4L1 = 23.56 A XNO9L1 = -2.12 A	Ring 4	XNO4L1 = 15.75 A XNO9L1 = -20.05 A
Ring 3	XNO4L1 = 10.53 A XNO9L1 = -16.76 A	Ring 3	XNO4L1 = 10.02 A XNO9L1 = -17.19 A
Ring 2	XNO4L1 = 17.04 A XNO9L1 = -3.73 A	Ring 2	XNO4L1 = 21.48 A XNO9L1 = -17.18 A
Ring 1	XNO4L1 = -3.84 A XNO9L1 = -2.56 A	Ring 1	XNO4L1 = 7.16 A XNO9L1 = -5.73 A

Table 3.7: Compensating normal sextupole corrector magnet currents for individual 3rd order normal resonance compensation with the alternative octupole configuration in Table 3.6 in all rings.

2Qx+Qy	XSK+OCT	3Qy	XSK + OCT
Ring 4	XSK2L4 = 3.44 A XSK6L4 = 1.83 A	Ring 4	XSK2L4 = -2.89 A XSK6L4 =1.78 A
Ring 3	XSK2L4 = 6.44 A XSK6L4 = 5.66 A	Ring 3	XSK2L4 = -3.83 A XSK6L4 = 4.33 A
Ring 2	XSK2L4 = 13.95 A XSK6L4 = 0.17 A	Ring 2	XSK2L4 = -1.06 A XSK6L4 = 3.61 A
Ring 1	XSK2L4 = 1.83 A XSK6L4 = -2.06 A	Ring 1	XSK2L4 = -8.61 A XSK6L4 = 3.28 A

Table 3.8: Compensating skew sextupole corrector magnet currents for individual 3rd order skew resonance compensation with the alternative octupole configuration in Table 3.6 in all rings.

3.2 Global resonance compensation

Based on the individual resonance compensation settings for all resonances in all rings, a global resonance compensation scheme can be used to compensate all resonances simultaneously. For 3^{rd} order resonances, the process for global resonance compensation described in [5] is followed. The transfer matrix in Eq. 3.1 is constructed with the corrector magnets RDTs for both resonances obtained with PTC in MADX. The subscript denotes the corresponding resonance ($30 \coloneqq 3Q_x, 12 \coloneqq Q_x + 2Q_y$) and the superscript indicates which corrector magnet is used. The column vector on the right-hand side is filled using the real and imaginary part of the corrector RDTs obtained from individually compensating each resonance.

$$\underbrace{\begin{bmatrix} Re[RDT^1_{30}] & Re[RDT^2_{30}] & Re[RDT^3_{30}] & Re[RDT^4_{30}] \\ Im[RDT^1_{30}] & Im[RDT^2_{30}] & Im[RDT^3_{30}] & Im[RDT^4_{30}] \\ Re[RDT^1_{12}] & Re[RDT^2_{12}] & Re[RDT^3_{12}] & Re[RDT^4_{12}] \\ Im[RDT^1_{12}] & Im[RDT^2_{12}] & Im[RDT^3_{12}] & Im[RDT^4_{12}] \end{bmatrix}}_{Correctors} \times \underbrace{\begin{bmatrix} F^1 \\ F^2 \\ F^3 \\ F^4 \end{bmatrix}}_{Currents} = \underbrace{\begin{bmatrix} Re[RDT_{30}] \\ Im[RDT_{30}] \\ Re[RDT_{12}] \\ Im[RDT_{12}] \end{bmatrix}}_{Resonances} \tag{3.1}$$

Solving the above for the two normal resonances, one can obtain a configuration using a set of normal corrector magnets that both normal resonances simultaneously. If the solution using four magnets requires currents which can not be exceeded in the machine, more or less magnets can be used. In these cases, the transfer matrix can be transformed into a square matrix using using singular value decomposition (SVD). While the system of equations is solvable using SVD, the solution will be approximate and the settigs can achieve only partial resonance compensation. For skew resonance compensation, only three skew corrector magnets are equipped with a power supply and thus the solutions obtained for global skew resonance compensation are approximate in all rings.

3.2.1 Global 3^{rd} order resonance compensation

The compensating settings for both normal and skew 3^{rd} resonances for all rings with different numbers of corrector magnets are shown in Tables 3.9 to 3.12. As the sextupole corrector magnets can be powered with currents of up to 50 A, it is necessary to use more or less magnets if the required currents exceed this limit, thus the solutions for any number of available magnets are shown. For the normal resonances, an exact solution using four magnets was found only in ring 3. In the other rings, only partial global resonance compensation can be achieved. For the skew resonances, only three corrector magnets are equipped with a power supply, thus global resonance compensation is partial in all rings. However, adding the additional skew corrector magnet XSK9L1 would allow for full global skew resonance compensation in all rings.

The compensating RDT for each resonances when using the global resonance compensation configuration can be calculated with MADX and expressed in terms of the two corrector magnets previously used for individual resonance compensation. This can be used to see how the magnets in the global resonance compensation

Correctors	Normal correctors	Expected Losses	Skew correctors	Expected Losses
6	XNO4 = -18.02 A XNO6 = 40.78 A XNO9 = 35.52 A XNO12 = -59.50 A XNO311 = -46.16 A XNO816 = 5.00 A			
5	XNO4 = -56.10 A XNO9 = -62.42 A XNO12 = 40.12 A XNO311 = -60.83 A XNO816 = -2.64 A			
4	XNO6 = 65.32 A XNO12 = -81.80 A XNO311 = -29.70 A XNO816 = 8.79 A	3Qx: 0.80 % Qx+2Qy: 0.44 %	XSK2L4= -13.47 A XSK4L1= 20.85 A XSK6L4= 2.87 A XSK9L1 = -18.46 A	3Qy: 0.40 % Qx+2Qy: 0.46 %
3	XNO12 = 13.51 A XNO311 = -31.30 A XNO816 = -31.84 A	3Qx:5.23% Qx+2Qy: 0.50 %	XSK2L4= -9.74 A XSK4L1= 16.11 A XSK6L4= -3.11 A	3Qy: 4.73 % 2Qx+Qy:0.77%

Table 3.9: Different global 3^{rd} order resonance compensation settings in ring 1

settings drive each of the resonances and how close they are to the respective individual resonance compensation. The losses in terms of corrector magnet currents when crossing individual resonances can be seen in Figs. 3.21 to 3.24. These plots include both the individual and the global resonance compensation configuration from Tables 3.9 to 3.12, which allows for the extrapolation of the expected losses.

Correctors	Normal correctors	Expected Losses	Skew correctors	Expected Losses
6	XNO4 = -27.04 A XNO6 = 62.25 A XNO9 = 39.18 A XNO12 = -80.62 A XNO311 = -98.46 A XNO816 = 45.92 A			
5	XNO4 = -29.60 A XNO6 = 65.70 A XNO12 = -108.88 A XNO311 = -88.17 A XNO816 = 45.62 A			
4	XNO6 = 96.83 A XNO12 = -104.06 A XNO311 = -77.79 A XNO816 = 51.53 A	3Qx: 0.80 % Qx+2Qy: 0.25 %	XSK2L4= -7.01 A XSK4L1= 31.30 A XSK6L4= 1.73 A XSK9L1 = -16.94 A	3Qy: 1.10 % Qx+2Qy: 0.76 %
3	XNO6 = -42.44 A XNO311 = 58.63 A XNO816 = -70.13 A	3Qx: 17.20 % Qx+2Qy: 0.85 %	XSK2L4= -3.59A XSK4L1= 26.95 A XSK6L4= -3.76 A	3Qy: 6.91 % 2Qx+Qy: 3.05 %

Table 3.10: Different global 3rd order resonance compensation settings in ring 2

Correctors	Normal correctors	Expected Losses	Skew correctors	Expected Losses
6	XNO4 = -5.43 A XNO6 = 16.38 A XNO9 = 3.03 A XNO12 = -15.56 A XNO311 = -37.45 A XNO816 = 19.33 A			
5	XNO6 = 22.01 A XNO9 = 3.54 A XNO12 = -14.31 A XNO311 = -35.69 A XNO816 = 20.41 A			
4	XNO6 = 22.57 A XNO12 = -16.83 A XNO311 = -34.68 A XNO816 = 20.43 A	3Qx: 0.40 % Qx+2Qy: 0 %	XSK2L4= -7.85 A XSK4L1= 24.49 A XSK6L4= 2.74 A XSK9L1 = -3.86 A	3Qy: 0.61 % Qx+2Qy: 0.84 %
3	XNO12 = 11.17 A XNO311 = -46.49 A XNO816 = 44.78 A	3Qx: 6.08 % Qx+2Qy: 1.66 %	XSK2L4= -7.07 A XSK4L1= 23.50 A XSK6L4= 1.49 A	3Qy: 0.81 % 2Qx+Qy: 1.03%

Table 3.11: Different global 3rd order resonance compensation settings in ring 3

Correctors	Normal correctors	Expected Losses	Skew correctors	Expected Losses
6	XNO4 = -29.51 A XNO6 = 60.81 A XNO9 = 10.04 A XNO12 = -52.08 A XNO311 = -129.66 A XNO816 = 97.48 A			
5	XNO6 = 101.48 A XNO9 = 20.44 A XNO12 = -54.38 A XNO311 = -121.58 A XNO816 = 108.93 A			
4	XNO6 = 104.69 A XNO12 = -68.91 A XNO311 = -115.74 A XNO816 = 109.04 A	3Qx: 0.46 % Qx+2Qy:1.06 %	XSK2L4= -5.86 A XSK4L1= 13.99 A XSK6L4= -0.03 A XSK9L1 = -3.65 A	3Qy: 0.50 % Qx+2Qy: 0.55 %
3	XNO9 = -21.76 A XNO311 = -43.07 A XNO816 = 39.25 A	3Qx: 7.87% % Qx+2Qy: 1.24% %	XSK2L4= -5.12 A XSK4L1= 13.05 A XSK6L4= -1.21 A	3Qy: 0.80% 2Qx+Qy: 0.61%

Table 3.12: Different global 3rd order resonance compensation settings in ring 4

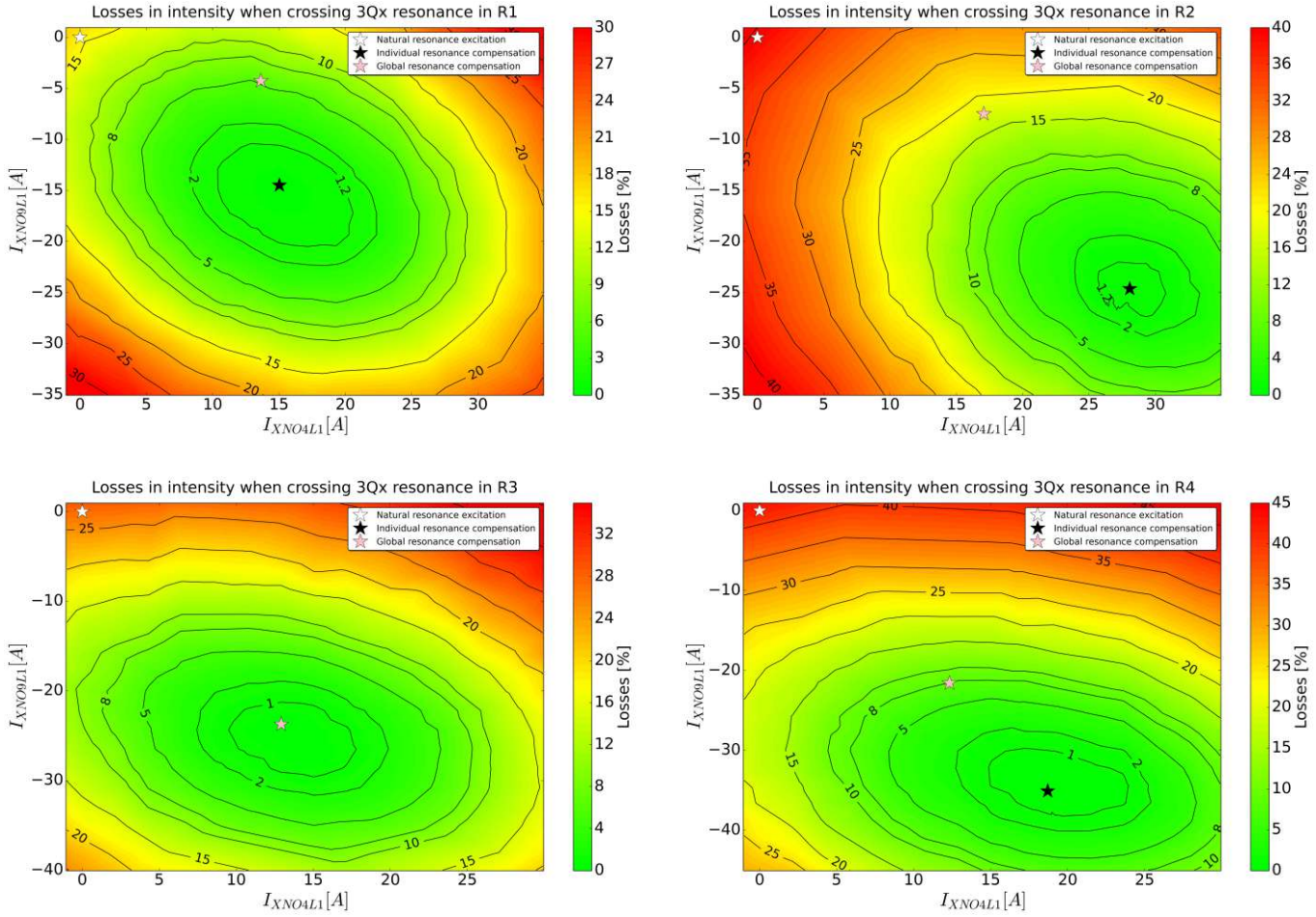

Figure 3.21: Color-coded losses when crossing the $3Q_x$ resonance in all rings with different current configurations, the compensation is marked by the black star, the pink star represents the $3Q_x$ resonance compensation with the global configuration and the white star marks the natural resonance excitation.

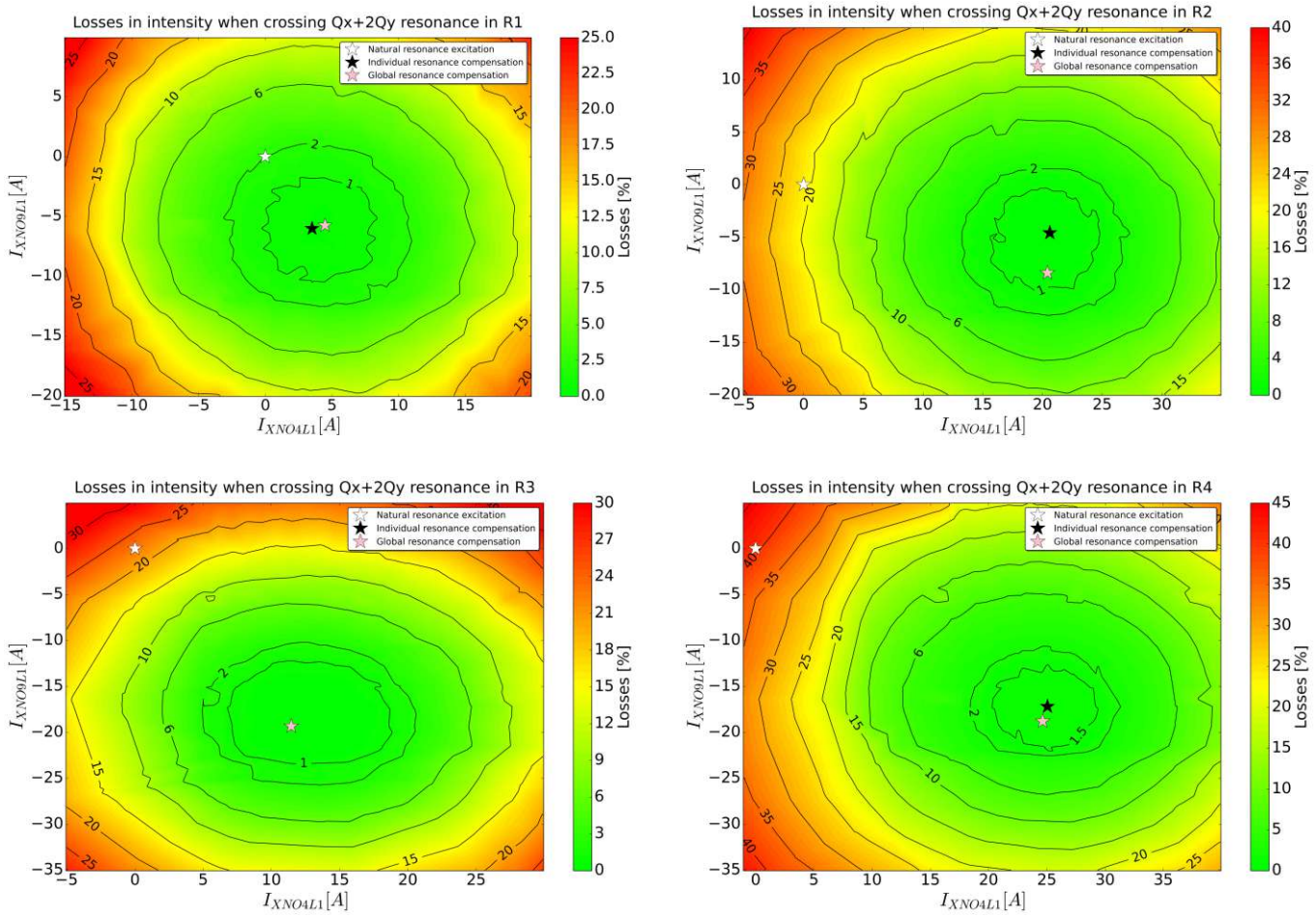

Figure 3.22: Color-coded losses when crossing the $Q_x + 2Q_y$ resonance in all rings with different current configurations, the compensation is marked by the black star, the pink star represents the $Q_x + 2Q_y$ resonance compensation with the global configuration and the white star marks the natural resonance excitation.

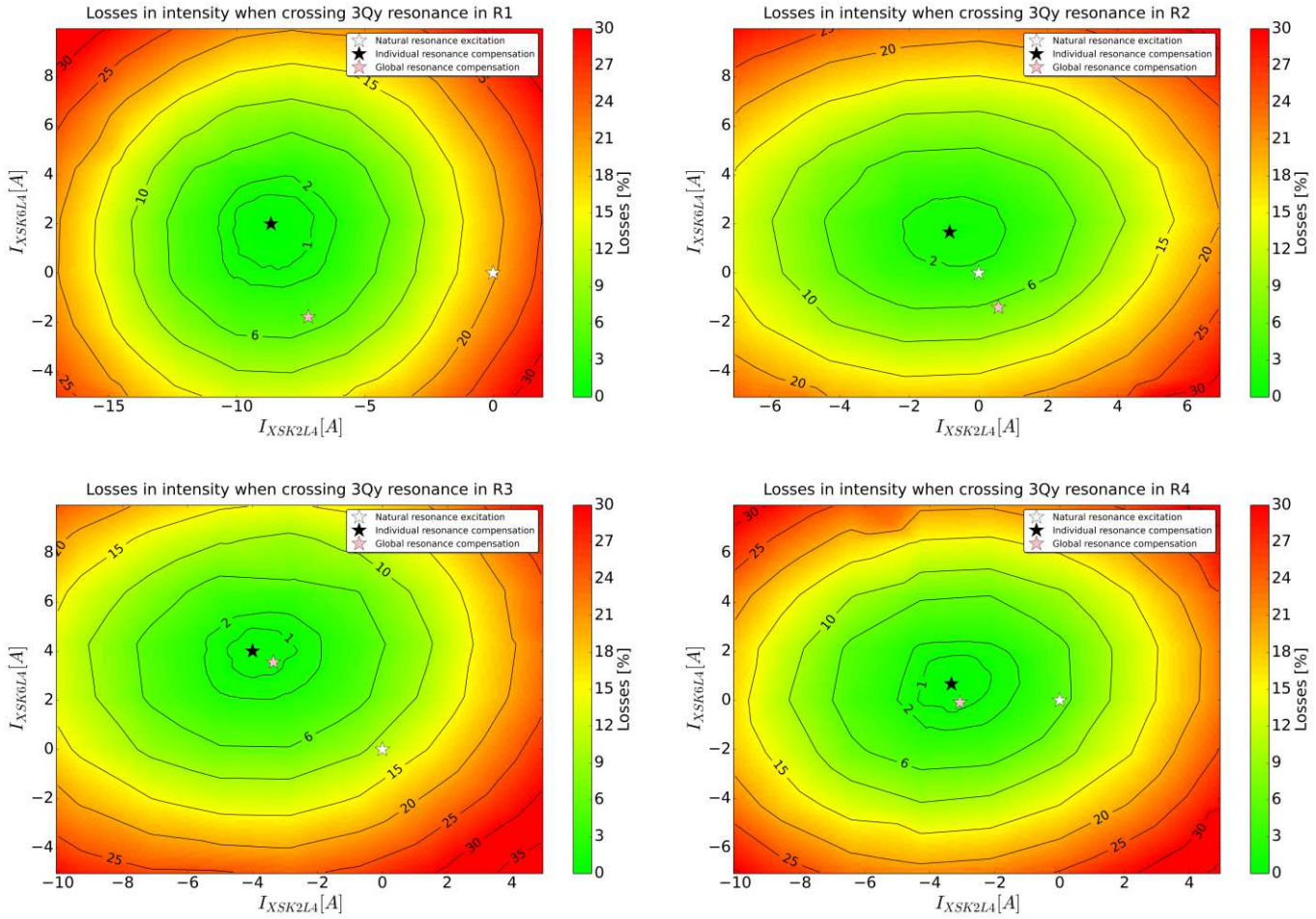

Figure 3.23: Color-coded losses when crossing the $3Q_y$ resonance in all rings with different current configurations, the compensation is marked by the black star, the pink star represents the $3Q_y$ resonance compensation with the global configuration and the white star marks the natural resonance excitation.

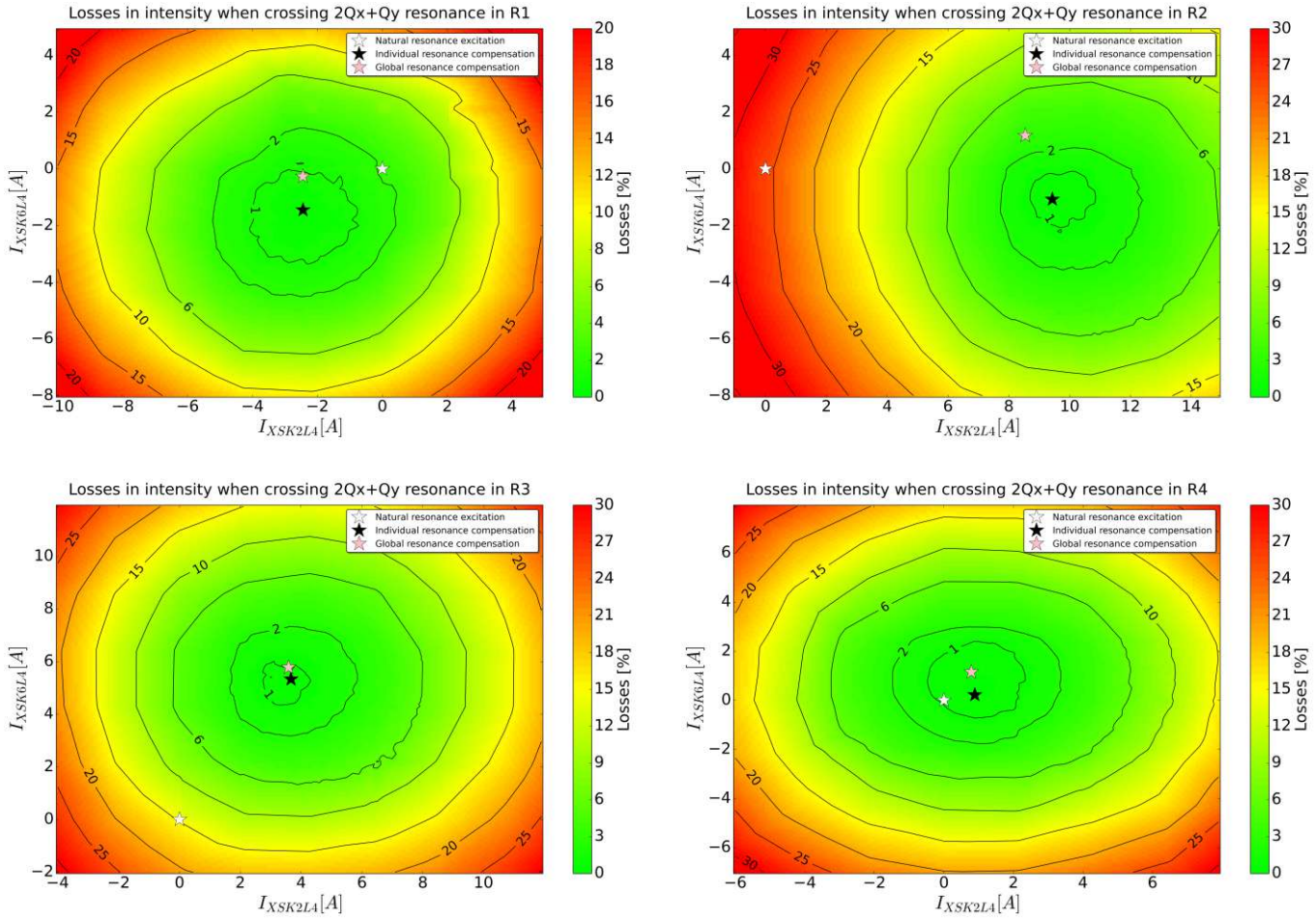

Figure 3.24: Color-coded losses when crossing the $2Q_x + Q_y$ resonance in all rings with different current configurations, the compensation is marked by the black star, the pink star represents the $2Q_x + Q_y$ resonance compensation with the global configuration and the white star marks the natural resonance excitation.

3.2.2 Global compensation of 3^{rd} and 4^{th} order resonances

Similarly to the process of global 3^{rd} order resonance compensation, global compensation settings based on the individual $3^{\text{rd}} + 4^{\text{th}}$ order resonance compensation can be found by solving the system of equations 3.1. The octupoles are powered with the settings given in Table 3.6 on the left. The solutions using different numbers of normal and skew corrector sextupoles in all rings are summarized in Tables 3.13 to 3.16. Expressing the global compensation RDTs using only one set of magnets allows for an estimation of the remnant losses which are shown in Figs 3.25 and 3.26 for the two normal resonances $3Qx$ and $Q_x + 2Q_y$ and Figs 3.27 and 3.28 for the skew resonances $3Q_y$ and $2Q_x + Q_y$ respectively

In rings 1 and 3, a set of four normal correctors can be used to fully compensate both normal resonances. In rings 2 and 4, it was not possible to find an exact solution using four normal corrector magnets, thus a configuration obtained through SVD was used instead. This solution is approximate and both resonances are only partially compensated.

Like for the 3^{rd} order skew resonances without octupoles, adding the skew sextupole XSK9L1 would allow for full global compensation of skew 3^{rd} order resonances in all rings. Comparing the expected losses when using three and four corrector magnets, one can see the improved compensation that an additional skew corrector magnet would offer.

Number of correctors	Normal correctors	Losses	Skew correctors	Losses
6	XNO4 = -6.07 A XNO6 = 14.71 A XNO9 = 22.04 A XNO12 = -28.62 A XNO311 = -1.70 A XNO816 = -20.71 A			
5	XNO6 = 59.47 A XNO9 = 37.21 A XNO12 = -55.37 A XNO311 =-40.33 A XNO816 = 8.59 A			
4	XNO6 = 20.86 A XNO9 = 23.54 A XNO12 = -26.57 A XNO816 = -19.51 A	3Qx: 1.23 % Qx+2Qy: 0.79 %	XSK2L4 = -16.37 A XSK4L1 = 33.49 A XSK6L4 = 4.18 A XSK9L1 = -26.26 A	3Qy: 0.17 % 2Qx+Qy: 1.48 %
3			XSK2L4= -11.07 A XSK4L1= 26.75 A XSK6L4= -4.33 A	3Qy: 6.24% 2Qx+Qy: 2.38%

Table 3.13: Different global 3^{rd} and 4^{th} order resonance compensation settings in ring 1

Number of correctors	Normal correctors	Losses	Skew correctors	Losses
6	XNO4 = -19.80 A XNO6 = 45.76 A XNO9 = 25.85 A XNO12 = -57.36 A XNO311 = -78.12 A XNO816 = 41.98 A			
5	XNO6 = 90.27 A XNO9 = 41.72 A XNO12 = -74.43 A XNO311 = -89.71 A XNO816 = 51.31 A			
4	XNO6 = 70.64 A XNO12 = -72.50 A XNO311 = -63.79 A XNO816 = 46.08 A	3Qx: 1.77 % Qx+2Qy: 1.20 %	XSK2L4 = -11.17 A XSK4L1 = 48.93 A XSK6L4 = 3.08 A XSK9L1 = -25.79 A	3Qy: 0.61 %: 2Qx+Qy: 1.48%
3	XNO6 = 23.72 A XNO12 -51.02 A XNO311 = -21.52 A	3Qx: 4.45 % Qx+2Qy: 1.30 %	XSK2L4 = -5.97 A XSK4L1 = 42.31 A XSK6L4 = -5.28 A	3Qy: 8.88% 2Qx+Qy: 2.08%

Table 3.14: Different global 3^{rd} and 4^{th} order resonance compensation settings in ring 2

Number of correctors	Normal correctors	Losses	Skew correctors	Losses
6	XNO4 = 4.61 A XNO6 = -2.65 A XNO9 = -6.69 A XNO12 = 4.82 A XNO311 = -10.05 A XNO816 = 4.60 A			
5	XNO6 = 22.01 A XNO9 = 3.54 A XNO12 = -14.31 A XNO311 = -35.69 A XNO816 = 20.41 A			
4	XNO6 = 22.57 A XNO12= -16.83 A XNO311 = -34.68 A XNO816 = 20.43 A	3Qx: 1.79 % Qx+2Qy: 1.14 %	XSK2L4 = -9.70 A XSK4L1 = 34.26 A XSK6L4 = 2.13 A XSK9L1 = -5.59 A	3Qy: 0.20 % 2Qx+Qy: 1.01 %
3			XSK2L4 = -8.57 A XSK4L1 = 32.83 A XSK6L4 = 0.32 A	3Qy: 0.47 % 2Qx+Qy: 1.66 %

Table 3.15: Different global 3^{rd} and 4^{th} order resonance compensation settings in ring 3

Number of correctors	Normal correctors	Predicted Losses	Skew correctors	Losses
6	XNO4 = -33.76 A XNO6 = 66.46 A XNO9 = 17.28 A XNO12 = -62.12 A XNO311 = -132.52 A XNO816 = 102.19 A			
5	XNO6 = 91.41 A XNO9 = 12.81 A XNO12 = -45.32 A XNO311 = -120.11 A XNO816 = 103.37 A			
4	XNO6 = 93.42 A XNO12 = -54.411 A XNO311 = -116.45 A XNO816 = 103.44 A	3Qx: 0.80 % Qx+2Qy: 1.47 %	XSK2L4= -6.71 A XSK4L1= 20.96 A XSK6L4= 0.79 A XSK9L1 = -5.83 A	3Qy: 0.19 % Qx+2Qy: 1.40 %
3	XNO9 = -21.76 A XNO311 = -43.07 A XNO816 = 39.25 A	3Qx: 6.08%% Qx+2Qy: 1.66%%	XSK2L4= -5.54 A XSK4L1= 19.47 A XSK6L4= -1.10 A	3Qy: 0.34 % 2Qx+Qy: 1.65%

Table 3.16: Different global 3^{rd} and 4^{th} order resonance compensation settings in ring 4

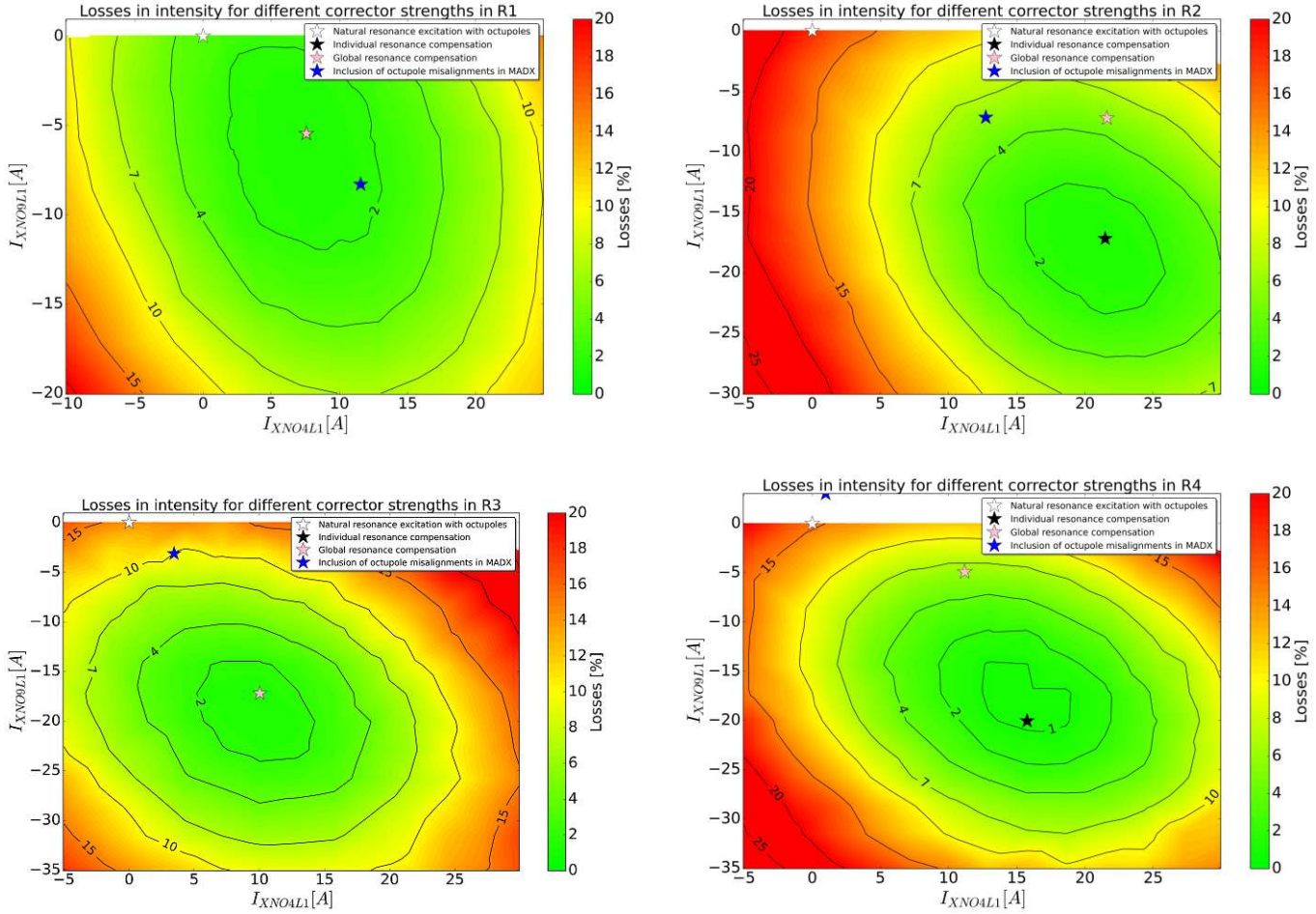

Figure 3.25: Color-coded losses when crossing the $3Q_x$ resonance with 4^{th} order resonance compensation in all rings with different current configurations. The individual compensation is marked by the black star, the pink star represents the global resonance compensation with the configuration from 3.17 and the white star marks the natural resonance excitation.

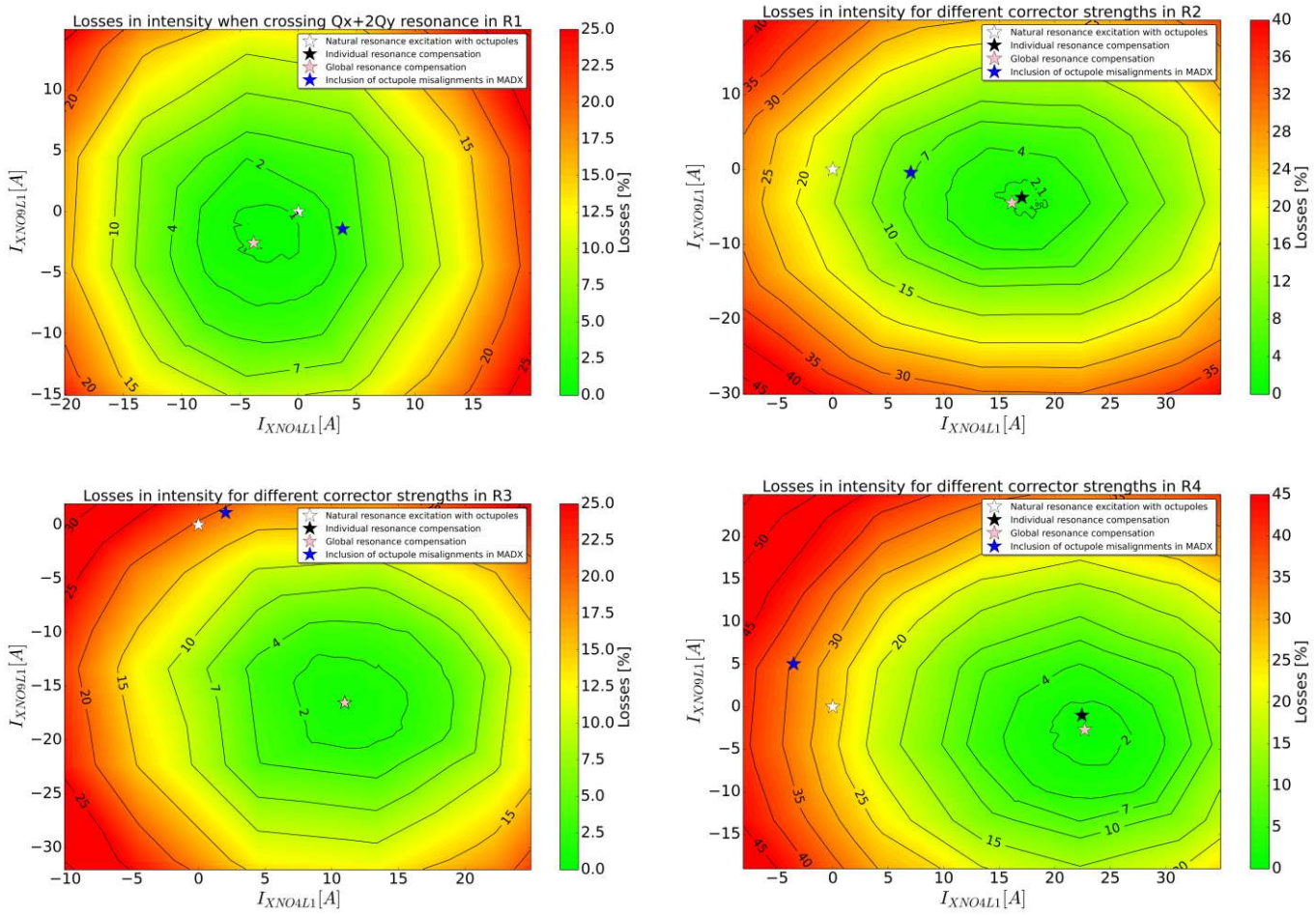

Figure 3.26: Color-coded losses when crossing the $Q_x + 2Q_y$ resonance with 4^{th} order resonance compensation in all rings with different current configurations. The individual compensation is marked by the black star, the pink star represents the global resonance compensation with the configuration from 3.17 and the white star marks the natural resonance excitation.

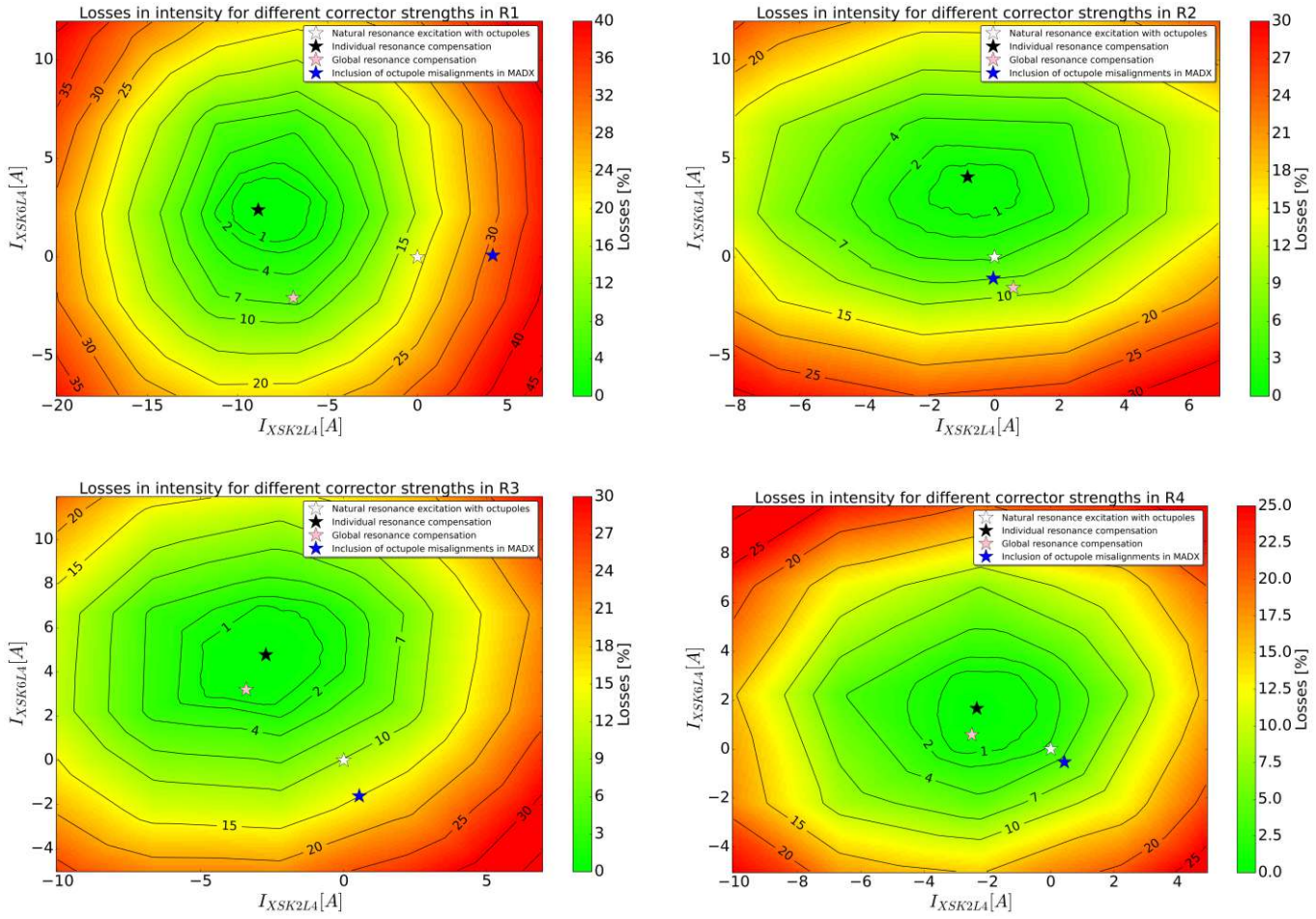

Figure 3.27: Color-coded losses when crossing the $3Q_y$ resonance with 4^{th} order resonance compensation in all rings with different current configurations. The individual compensation is marked by the black star, the pink star represents the global resonance compensation with the configuration from 3.17 and the white star marks the natural resonance excitation.

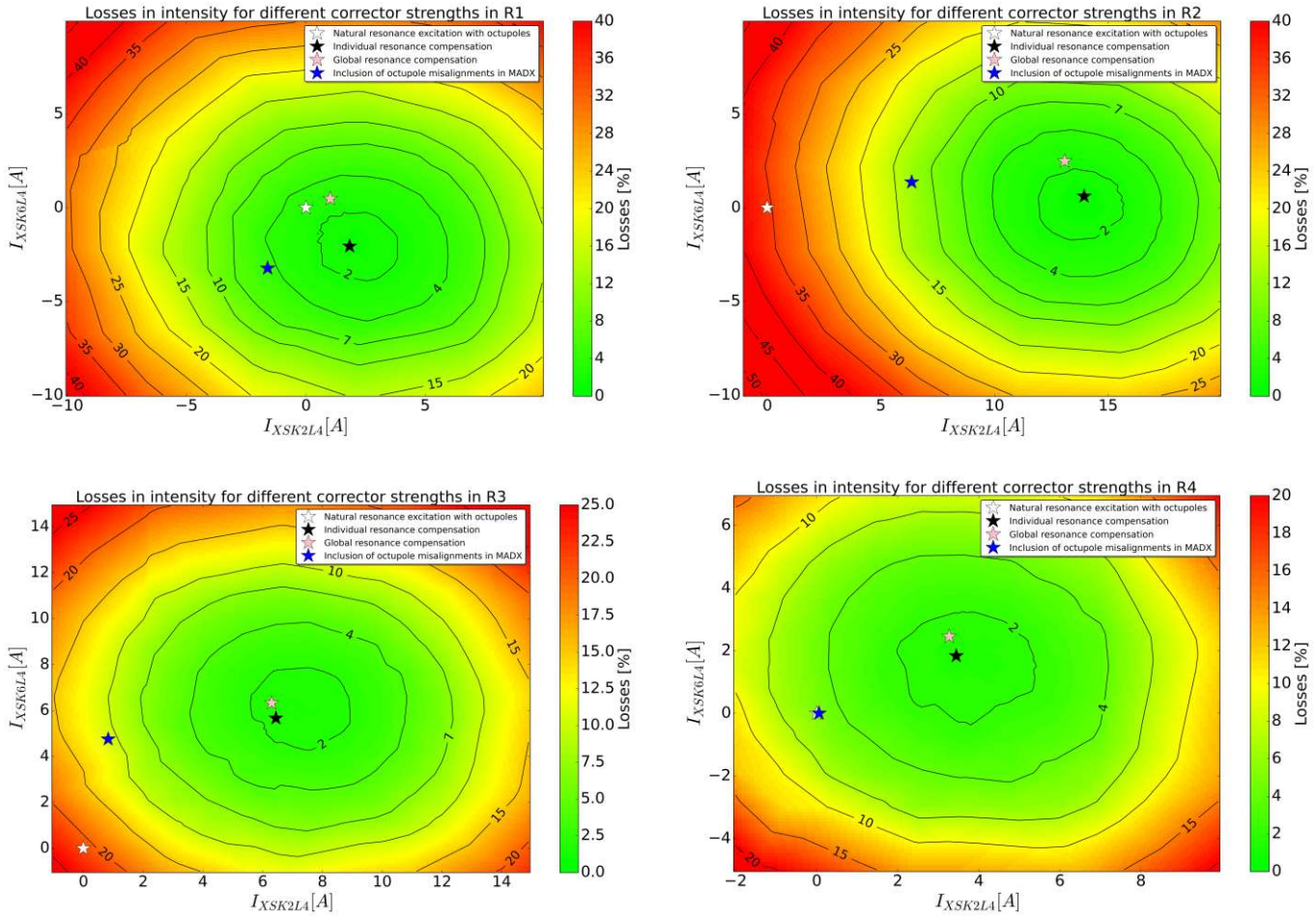

Figure 3.28: Color-coded losses when crossing the $2Q_x + Q_y$ resonance with 4^{th} order resonance compensation in all rings with different current configurations. The individual compensation is marked by the black star, the pink star represents the global resonance compensation with the configuration from 3.17 and the white star marks the natural resonance excitation.

Ring	Normal sextupoles	Skew sextupoles	Normal octupoles
1	XNO6 = 20.86 A XNO9 = 23.54 A XNO12 = -26.57 A XNO816 = -19.51 A	XSK2L4 = -11.07 A XSK4L1 = 26.75 A XSK6L4 = -4.33 A	ONO4L1 = -8.55 A ONO12L1 = -50 A ONO311L1 = 74.7 A ONO816L1 = 40.05 A
2	XNO6 = 23.72 A XNO12 = -50 A XNO311 = -21.52 A	XSK2L4 = -5.97 A XSK4L1 = 42.31 A XSK6L4 = -5.28 A	ONO4L1 = -7.52 A ONO12L1 = -50 A ONO311L1 = 65.59 A ONO816L1 = 46.95 A
3	XNO6 = -8.55 A XNO12 = 8.82 A XNO311 = -13.57 A XNO816 = 3.64 A	XSK2L4 = -8.57 A XSK4L1 = 32.83 A XSK6L4 = 0.32 A	ONO4L1 = -6.6 A ONO12L1 = -43.52 A ONO311L1 = 57.59 A ONO816L1 = 34.97 A
4	XNO9 = -21.76 A XNO311 = -43.07 A XNO816 = 39.25 A	XSK2L4 = -5.54 A XSK4L1 = 19.47 A XSK6L4 = -1.10 A	ONO4L1 = -7.13 A ONO12L1 = -48.82 A ONO311L1 = 62.24 A ONO816L1 = 39.59 A

Table 3.17: Corrector magnet currents for global 3^{rd} and 4^{th} order resonance compensation in all rings.

3.2.3 Experimental validation of global resonance compensation

In order to confirm the predicted losses experimentally, each resonance was individually crossed using the best possible configuration in all rings summarized in Table 3.17. The losses were then compared to the estimations in Figures 3.25 to 3.28. The intensities with individual and global resonance compensation are summarized in Figure 3.29.

The global resonance compensation should be the same as the individual resonance compensation in rings 1 and 3 for both normal resonances while in rings 2 and 4, only partial normal resonance compensation is expected. It was observed that in ring 3, the estimated and measured losses using the global resonance compensation settings fully coincide. In all other rings, discrepancies between individual and global resonance compensation was observed. In ring 1, the losses using the global resonance compensation settings are worse than the individual resonance compensation. In rings 2 and 4, the observed individual and global resonance compensation is partial as expected with the accuracy of the prediction varying between different resonances.

The intensities while crossing all resonances in all rings with global resonance compensation and with no resonance compensation are depicted in Figure 3.30. The corresponding losses after crossing all resonances are summarized in Figure 3.31. The total reduction in losses when crossing all resonances with global resonance compensation ranges from 71.1 % in ring 2 to 93.4% in ring 3. Averaged over the four rings, the losses when crossing all resonances with natural resonance excitation are 23.5 % and with global resonance compensation they are 3.7%. Thus on average, global resonance compensation reduced the losses from crossing excited resonances by almost 85%.

The remaining losses can be attributed to the limited number of skew corrector magnets as well as current limitations in the normal corrector magnets.

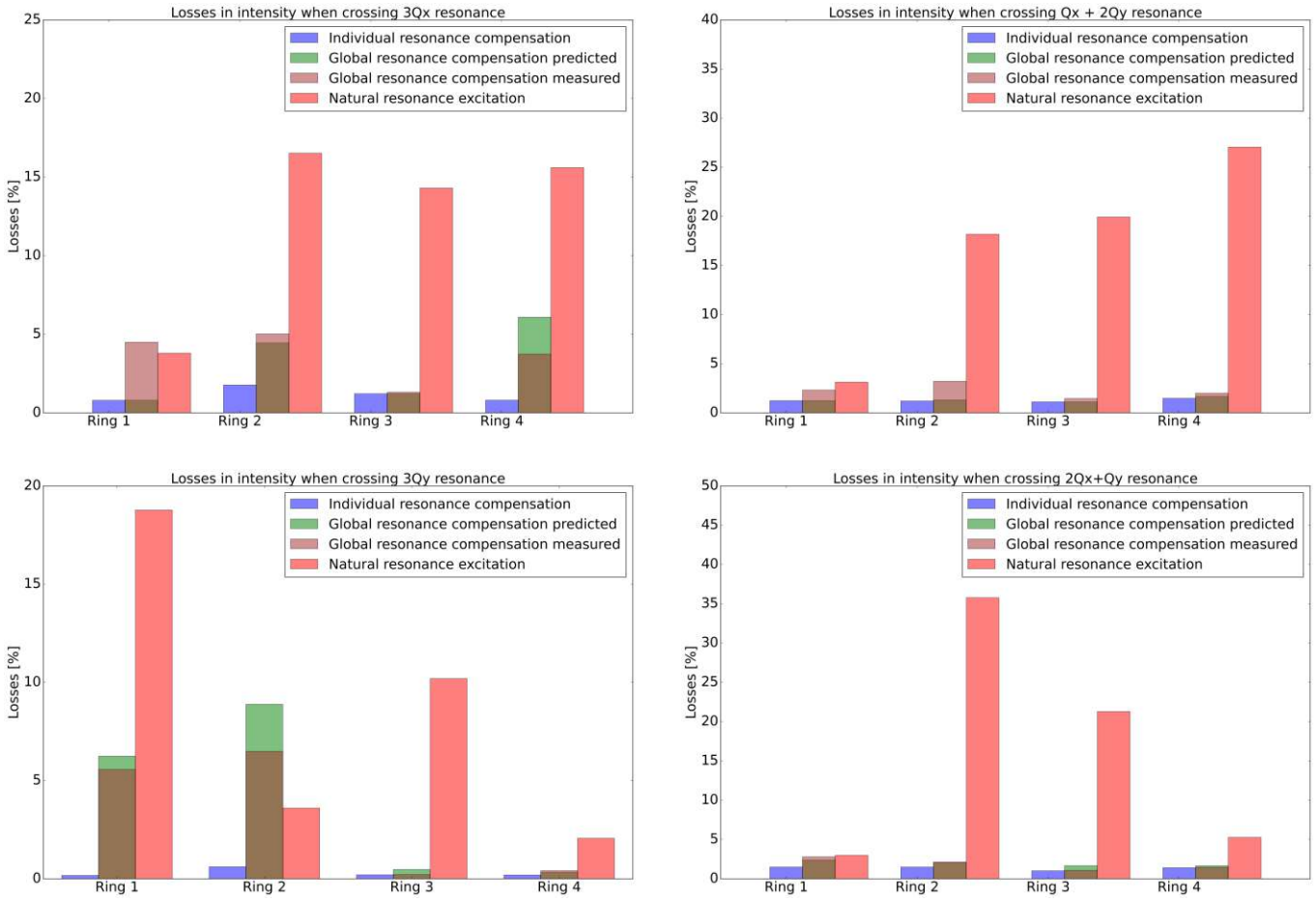

Figure 3.29: Losses when crossing each of the normal and skew 3^{rd} order resonance with 4^{th} order resonance compensation in all rings. The blue bar represents the measured losses with individual resonance compensation, the pink bar represents the measured losses with global resonance compensation using the configuration from table 3.17 and the red bar represents the measured losses with natural resonance excitation. The green bar represents the predicted losses using global resonance compensation configuration (pink stars in Figs. 3.25 to 3.28).

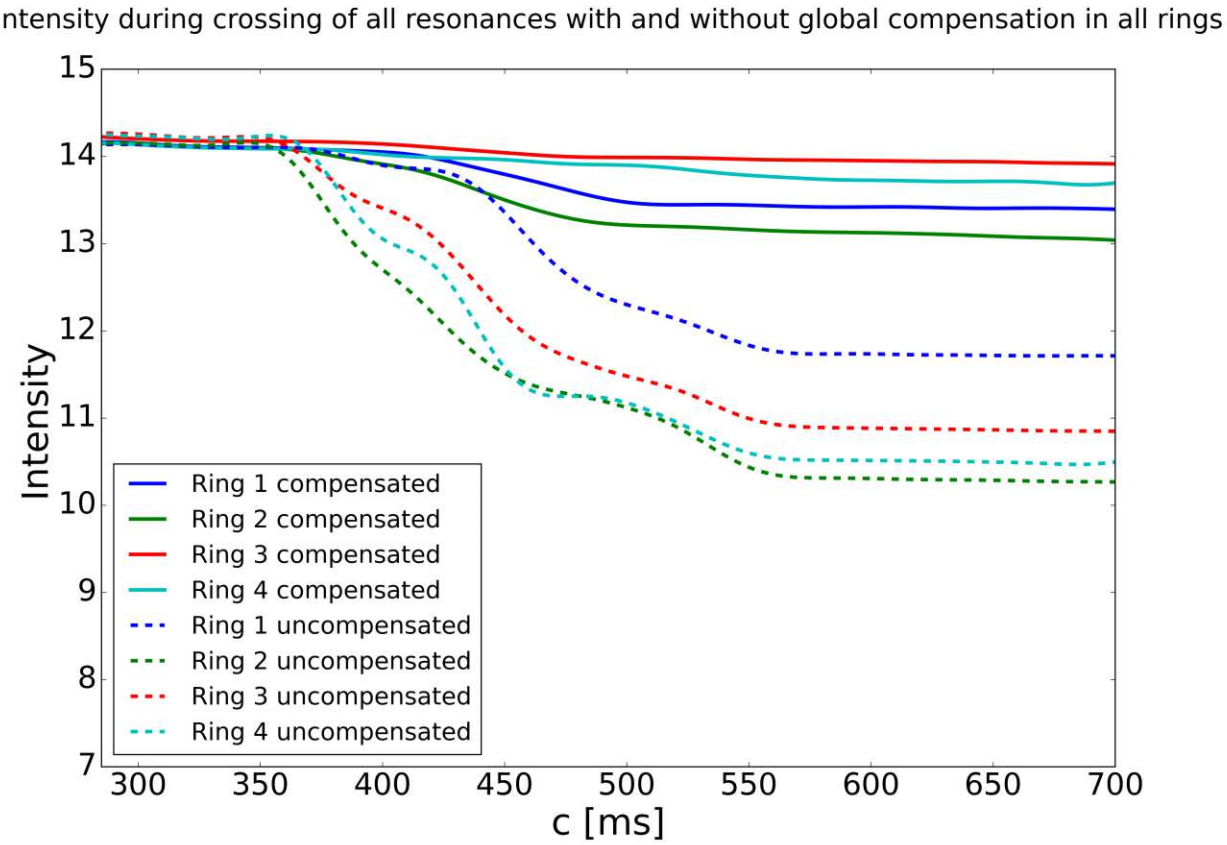

Figure 3.30: Intensity when crossing both normal and skew 3^{rd} order resonances and all normal 4^{th} order resonances with global resonance compensation settings (solid) and with natural resonance excitation in all rings (dashed).

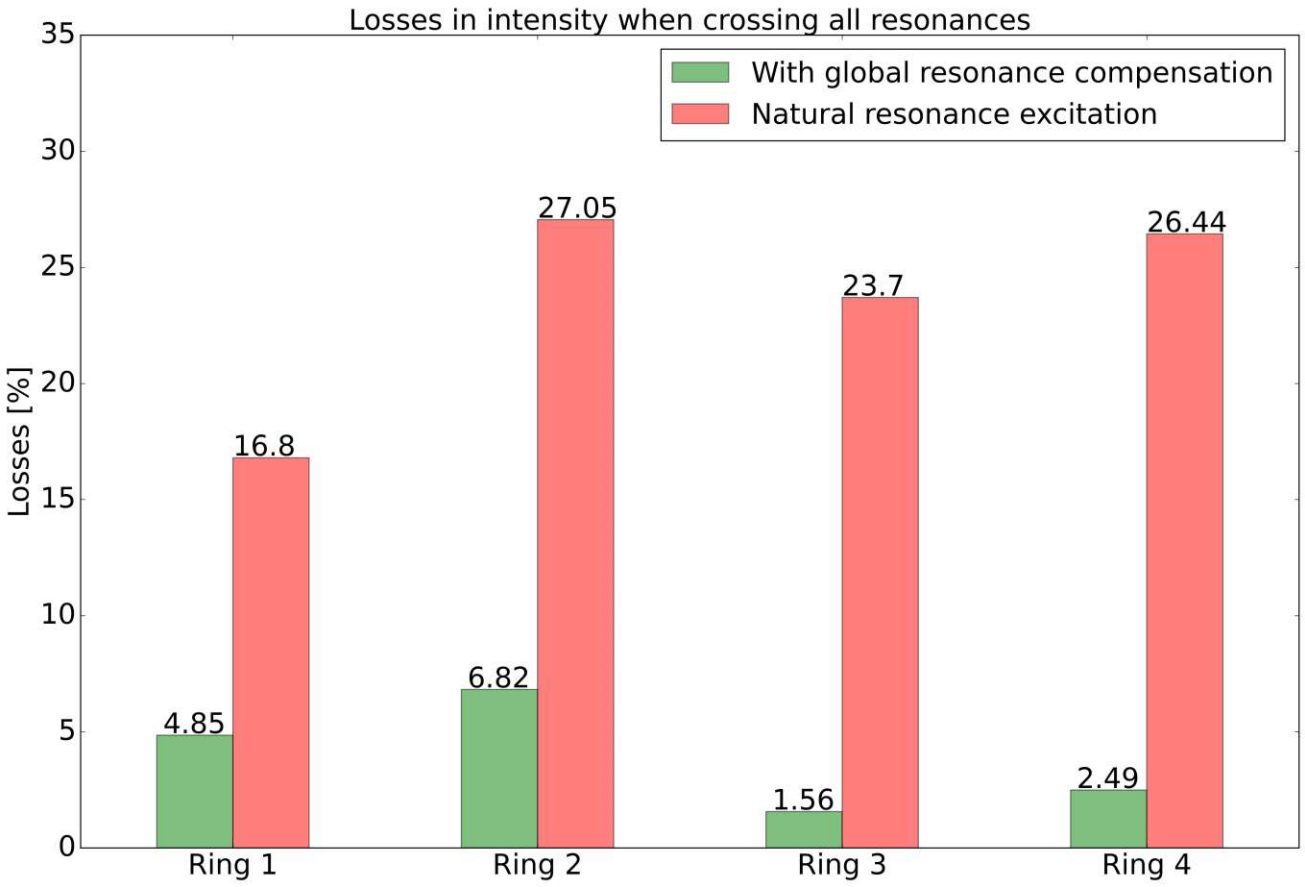

Figure 3.31: Losses crossing both normal and skew 3^{rd} order resonances and all normal 4^{th} order resonances with the global resonance compensation settings in all rings (green) and with no corrector magnets (red).

Chapter 4

Discussion

This study intended to show how 3^{rd} and 4^{th} order resonances in the PSB can be compensated individually and globally and how the compensation settings have changed compared to past studies. Further, the effect of chromaticity correction on non-systematic 3^{rd} order normal resonances has been studied in more detail.

Limitations

The approach used is based on minimizing the losses when crossing 3^{rd} and 4^{th} order resonances. Individually, all resonances can be fully compensated in all rings but global resonance compensation is limited, due to a limitation in the available magnets or currents. Most magnets can not be powered with currents of more than 50 A, which restricts the global resonance compensation of normal 3^{rd} order resonances. While there are six normal corrector sextupoles available, not more than four were used for global normal resonance compensation as using six magnets did not bring any advantage or reduce the power load per magnet.

Skew 3^{rd} order resonance compensation is limited due to only three skew corrector magnets being equipped with a power supply. Equipping a fourth skew sextupole, namely XSK9L1, with a power supply would allow for full global skew resonance compensation in all rings as can be seen in Tables 3.9.

4^{th} order resonances can be fully compensated in all rings and it was observed that the compensation settings for 3^{rd} order resonances are different if 4^{th} order resonances are compensated at the same time. It is not known how exactly octupoles affect 3^{rd} order resonances, but misaligned octupoles induce feed-down sextupolar magnetic fields from which drive 3^{rd} order resonances. The octupole misalignments in the PSB were measured and included in the magnet lattice modeled in MADX in the compensating configuration from Table 3.5. The 3^{rd} order RDTs including the feed-down sextupole fields were then calculated and compared to the measured 3^{rd} order resonances when both sextupoles and octupoles are used simultaneously. The measured and the calculated 3^{rd} order resonances do not coincide, thus it can be concluded that feed-down sextupolar fields from octupoles are not the main influence on the 3^{rd} order resonances. Compensating 3^{rd} and 4^{th} order resonances separately can not be used to find settings that compensate both 3^{rd} and 4^{th} order resonances si-

multaneously. Instead, each 3^{rd} resonance has to be compensated while the corrector octupoles are on.

It was also observed that if certain octupoles are used to compensate 4^{th} order resonances, $Q_x + 2Q_y$ resonance compensation is not possible anymore. While using certain octupoles, it looks like the $Q_x + 2Q_y$ resonance is split in two different resonances with different compensation settings as can be seen in Figure 3.26. The reason for this effect appearing when using only certain octupoles is not known and is subject to further investigation.

Previous studies

As these resonances are driven by magnetic field errors, they are different whenever there are changes in the magnet lattice, which has been observed in the past. Comparison of previous studies on resonance compensation with the current results shows how the resonance compensation settings have changed over time. In the PSB there have been some studies on resonance compensation over the last 20 years.

The first study on resonance compensation was done in 2003/2004[23] where corrector magnets have been used to compensate 3^{rd} order resonances. The comparison to this past study is limited as the working point at injection used to be different and the proton injection energy was at 50MeV instead of 160MeV. The compensated resonances in the study from 2003 were $3Q_y = 16$, $2Q_x + Q_y = 14$, $2Q_x - Q_y = 3$ and $Q_x + 2Q_y = 15$, none of which have been compensated in the current study. In 2004 however, the working point was changed to the one used in the current study and thus the same resonances had to be crossed and compensated during the tune change. There is one resonance that was compensated in both the current study and 20 years ago, which is the $3Q_y = 13$ resonance in ring 1. In the study from 2004, this resonance was compensated with vertical chromaticity correction, which affects 3^{rd} order resonances and limits the comparability of the two results. The compensating configuration from 2004 for the $3Q_y = 13$ resonance in ring 1 did not change very significantly and compensating this resonance again with vertical chromaticity correction in a further study could reveal how much of the change can be attributed to chromaticity correction. The $3Q_y = 13$ resonance was also crossed in 2004 in ring 2 but no losses were observed and there was no compensation. Rings 3 and 4 were not part of the study from 2004.
The next study on resonance compensation in the PSB is from 2018[22] before LIU[28, 29], which was the most recent major upgrade of the PSB. Comparing the resonance compensation before and after LIU shows that there are resonances that were not observed in all rings prior to LIU. The 3^{rd} order resonances that were observed already before LIU have changed in all rings by varying degrees. Further, 4^{th} order resonance compensation has not been observed prior to LIU.

In the study on resonance compensation from 2021, all 3^{rd} and 4^{th} order resonances have been observed for the first time [27]. All resonances were different compared to the pre-LIU study, which is not surprising due to the major changes in the magnet lattice of the PSB. Using the global resonance compensation scheme all resonances could be compensated to varying degrees, however remnant losses from some resonances in some rings were observed due to limitations in magnets.

Conclusion

In this study, it was shown that individual 3^{rd} and 4^{th} order resonances can be fully compensated using pairs of different types of corrector magnets in all rings. Further, based on the settings for individual resonance compensation, a configuration using a larger set of magnets that globally compensates 3^{rd} and 4^{th} order resonances was found in each ring. These globally compensating settings were then tested with the operational cycle during which all resonances were crossed. The losses due to these resonances can be reduced significantly in all rings. Remnant losses, due to limitations in corrector magnets or currents, vary from ring to ring. The most remnant losses were measured in ring 2 with 6.8% and the best compensation was achieved in ring 3 with remnant losses of 1.5%.

List of Figures

Bibliography

[1] CERN. https://home.cern/science/physics/standard-model.

[2] CERN. https://home.cern/science/accelerators/accelerator-complex.

[3] CERN. https://home.cern/science/experiments/isolde.

[4] F. Asvesta and H. Bartosik, "Resonance driving terms from space charge potential," Tech. Rep., 2019.

[5] F. Asvesta *et al.*, "Resonance compensation for high intensity and high brightness beams in the CERN PSB," *JACoW HB*, vol. 2021, pp. 40–45, 2022. DOI: 10.18429/JACoW-HB2021-MOP06.

[6] I. Hofmann, "Stability of anisotropic beams with space charge," *Physical Review E*, vol. 57, no. 4, p. 4713, 1998. DOI: 10.1103/PhysRevE.57.4713.

[7] G. Franchetti, I. Hofmann, M. Giovannozzi, M. Martini, and E. Metral, "Space charge and octupole driven resonance trapping observed at the CERN proton synchrotron," *Physical Review Special Topics-Accelerators and Beams*, vol. 6, no. 12, p. 124 201, 2003. DOI: 10.1103/PhysRevSTAB.6.124201.

[8] E. Metral, G. Franchetti, M. Giovannozzi, I. Hofmann, M. Martini, and R. Steerenberg, "Observation of octupole driven resonance phenomena with space charge at the CERN proton synchrotron," *Nuclear Instruments and Methods in Physics Research Section A: Accelerators, Spectrometers, Detectors and Associated Equipment*, vol. 561, no. 2, pp. 257–265, 2006. DOI: 10.1016/j.nima.2006.01.029.

[9] H. Hotchi, H. Harada, and T. Takayanagi, "J-PARC RCS: High-order field components inherent in the injection bump magnets and their effects on the circulating beam during multi-turn injection," in *Journal of Physics: Conference Series*, IOP Publishing, vol. 1350, 2019, p. 012 102. DOI: 10.1088/1742-6596/1350/1/012102.

[10] S. Y. Lee, *Accelerator physics*. World Scientific Publishing Company, 2018.

[11] NIST. https://physics.nist.gov/cuu/Constants/index.html.

[12] H. Wiedemann, *Particle accelerator physics*. Springer Nature, 2015.

[13] B. Holzer, "Lattice design in high-energy particle accelerators," *arXiv preprint arXiv:1601.04913*, 2016.

[14] JUAS, "JUAS 2023 (course 1): The science of particle accelerators," Tech. Rep., 2023.

[15] K. Schindl, "Space charge," in *Beam measurement*, World Scientific, 1999, pp. 127–151.

[16] F. Asvesta *et al.*, "Identification and characterization of high order incoherent space charge driven structure resonances in the CERN proton synchrotron," *Physical Review Accelerators and Beams*, vol. 23, no. 9, p. 091 001, 2020. DOI: 10.1103/PhysRevAccelBeams.23.091001.

[17] F. Hinterberger, *Physik der Teilchenbeschleuniger und Ionenoptik*. Springer, 2008, vol. 2.

[18] G. Guignard, "The general theory of all sum and difference resonances in a three-dimensional magnetic field in a synchrotron," Tech. Rep., 1976.

[19] V. Kapin and F. Schmidt, "PTC modules for MAD-X code," Technical report, CERN, 2006. To be published, Tech. Rep.

[20] L. Deniau, H. Grote, G. Roy, F. Schmidt, and W. e. a. Herr, *Couplers for cavities*, http://mad.web.cern.ch/mad/.

[21] T. Prebibaj, F. Antoniou, G. Franchetti, H. Bartosik, and F. Asvesta, "Studies on the vertical half-integer resonance in the CERN PS booster," *JACoW IPAC*, vol. 2022, pp. 222–225, 2022.

[22] A. S. Garcia *et al.*, "Identification and compensation of betatronic resonances in the proton synchrotron booster at 160 mev," in *Proc. 10th Int. Particle Accelerator Conf.(IPAC'19)*, 2019, pp. 1054–1057. DOI: 10.18429/JACoW-IPAC2019-MOPTS086.

[23] P. Urschütz, "Measurement and compensation of betatron resonances at the CERN PS booster synchrotron," Ph.D. dissertation, Vienna, Tech. U., 2004.

[24] C. Gonzalez-Ortiz, R. Ainsworth, and P. Ostroumov, "Third-order resonance compensation at the FNAL recycler ring," Fermi National Accelerator Lab.(FNAL), Batavia, IL (United States), Tech. Rep., 2022. DOI: https://doi.org/10.18429/JACoW-IPAC2022-MOPOST050.

[25] F. Asvesta, H. Bartosik, A. Huschauer, Y. Papaphilippou, and G. Sterbini, "Resonance identification studies at the CERN PS," in *Journal of Physics: Conference Series*, IOP Publishing, vol. 1067, 2018, p. 062 021. DOI: 10.1088/1742-6596/1067/6/062021.

[26] H. Hotchi *et al.*, "J-PARC 3-GeV RCS: 1-MW beam operation and beyond," *Journal of Instrumentation*, vol. 15, no. 07, P07022, 2020. DOI: 10.1088/1748-0221/15/07/P07022.

[27] F. Asvesta *et al.*, "High intensity studies in the CERN proton synchrotron booster," *JACoW IPAC*, vol. 2022, pp. 2056–2059, 2022.

[28] J. Coupard *et al.*, "LHC injectors upgrade, technical design report," Tech. Rep., 2016. DOI: 10.17181/CERN.7NHR.6HGC.

[29] E. Shaposhnikova *et al.*, "LHC injectors upgrade (LIU) project at CERN," Tech. Rep., 2016. DOI: 10.18429/JACoW-IPAC2016-MOPOY059.

[30] F. A. et al., *Resonance and high intensity studies in the PSB*, https://indico.cern.ch/event/1107555/. (visited on 02/10/2022).

[31] V. Kain and N. Madysa, *Generic optimisation frontend and framework (geoff)*, https://gitlab.cern.ch/vkain/acc-app-optimisation.

[32] M. Powell, "The bobyqa algorithm for bound constrained optimization without derivatives.," 2009.

[33] B. M. C. Cartis J. Fiala and L. Roberts, "Improving the flexibility and robustness of model-based derivative-free optimization solvers," *ACM Transactions on Mathematical Software*, vol. 45:3, 32:1–32:41, 2019.

[34] L. R. C. Cartis and O. Sheridan-Methven, "Scaping local minima with derivative-free methods: A numerical investigation, optimization," 2021.